Incorporation of halogen (Cl, Br, I) in Li-P-S-O system for exploring new sulfide solid electrolytes with high conductivity and superior electrochemical performance in solid-state batteries

Hari Raj, Audric Neveu, Christian Jordy, Vincent Pelé, Valérie Pralong

To cite this version:

Hari Raj, Audric Neveu, Christian Jordy, Vincent Pelé, Valérie Pralong. Incorporation of halogen (Cl, Br, I) in Li-P-S-O system for exploring new sulfide solid electrolytes with high conductivity and superior electrochemical performance in solid-state batteries. Journal of Materials Chemistry A, 2024, ⟨10.1039/d4ta04904g⟩. ⟨hal-04784008⟩

HAL Id: hal-04784008
https://hal.science/hal-04784008v1

Submitted on 14 Nov 2024

Incorporation of halogen (Cl, Br, I) in Li-P-S-O system for exploring new sulfide solid electrolytes with high conductivity and superior electrochemical performance in solid-state batteries

Hari Raj [a,b]*, Audric Neveu*[a]*, Christian Jordy* [c]*, Vincent Pelé* [c] *and Valerie Pralong* [* a,b]

[a]Normandie Univ, Ensicaen, Unicaen, CNRS, Crismat, 14000 Caen, France.

[b]Réseau sur le Stockage Electrochimique de l'Énergie (RS2E), 80000 Amiens, France.

[c]SAFT, 111-113 Bd Alfred Daney 33074 Bordeaux, France.

***Corresponding Author:** valerie.pralong@ensicaen.fr

KEYWORDS: Solid-state batteries; sulfide solid electrolytes; halogen elements; electrochemical performance, XRD

ABSTRACT

The solid electrolytes (SEs) with high conductivity and better stability against lithium metal are most important requirements for successful commercialization of solid state battery (SSB) technology. Therefore, in the search for new SEs with above mentioned qualities, halogen elements (Cl, Br, I) are explored in Li-P-S-O system to prepare $Li_{10}GeP_2S_{12}$ (LGPS) structured SEs. In all prepared SEs, $Li_{3.3}PS_{3.7}O_{0.3}Br_{0.1}$ and $Li_{3.3}PS_{3.7}O_{0.3}I_{0.1}$ compositions show highest

conductivities of 0.77 mS cm^{-1} and 0.93(≈ 1.0) mS cm^{-1} at 25 °C. These compounds also show superior stability against lithium metal in symmetric cells as well as in full SSB cells tested with $LiNi_{0.8}Co_{0.15}Al_{0.05}O_2$ (NCA) cathode and graphite anode. The instability of sulfide based SEs in ambient environment is a major issue, whereas, our prepared compounds $Li_{3.3}PS_{3.7}O_{0.3}Br_{0.1}$ and $Li_{3.3}PS_{3.7}O_{0.3}I_{0.1}$ show 5 times higher stability in ambient environment conditions as compared to non-doped $Li_{3.2}PS_{3.7}O_{0.3}$. *In-situ* EIS study performed on full SSB as prepared and after charge-discharge cycles have revealed the contribution of interfacial reactions on impedance. The study also shows higher interfacial resistances in full SSB with Li-metal anode as compared graphite anode. At the end, post-mortem analysis of full SSB cell as well as SE-Li interfacial study was conducted by SEM and elemental mapping to observed the changes in the electrodes and electrolyte before and after charge-discharge cycles. Therefore, the present work reports sulfide based new SEs with high conducting and better stability, and their interfacial studies.

TABLE OF CONTENTS

“Increasing Li^+ ions conductivity with halogen elements”

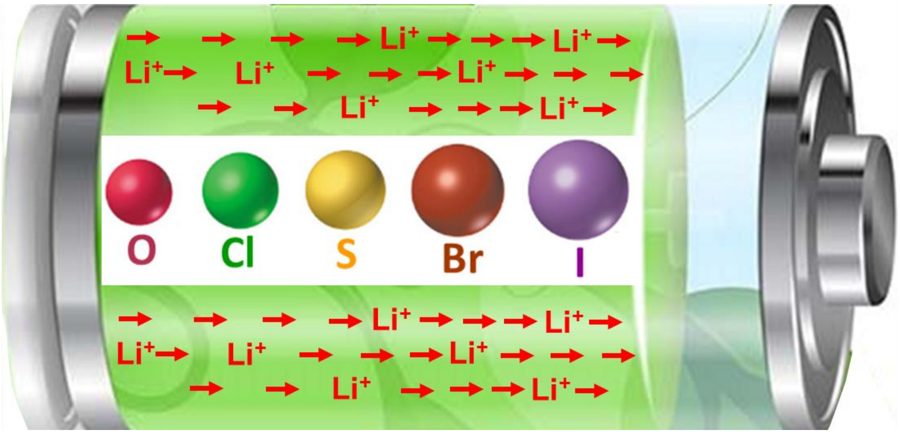

INTRODUCTION

Solid state batteries (SSBs) are considered to provide better safety as compared to Li-ion batteries because solid electrolytes (SEs) are used in SSBs instead of flammable organic liquid based electrolytes[1]. Furthermore, the final goal of SSBs is to use Li-metal directly as an anode for achieving high energy density[2,3]. However, dendrite formation in the Li-metal is a major issue in Li-ion batteries which is expected to be suppressed in SSBs due to the solid nature of electrolyte[4].

To achieve this goal, various types of solid electrolytes have already been reported for SSBs which can be divided into oxides, sulfides, halides, and polymers based on their properties, advantages, and disadvantages[5,6]. Among these solid electrolytes, sulfide based solid electrolytes have advantages over others due to high conductivity and ductile nature of sulfides[7,8]. Because of ductile nature of sulfide electrolytes, they provide more favorable conditions for solid state battery fabrication by just cold pressing without any further sintering process[9]. Kanno et al. reported a $Li_{10}GeP_2S_{12}$ called LGPS structured sulfide electrolyte exhibited ionic conductivity of 1.2×10^{-2} S cm^{-1} at room temperature which was comparable to the conductivity of organic liquid electrolytes[10,11]. Despite having high conductivity, $Li_{10}GeP_2S_{12}$ electrolyte suffers from poor cyclability in solid state batteries due to the reduction of Ge^{+4} ions to Ge^0 and instability against the lithium metal anode. Moreover, germanium (Ge) is a rare and expensive element, which limits the industrial application of $Li_{10}GeP_2S_{12}$[12–14]. To overcome the issues of $Li_{10}GeP_2S_{12}$ solid electrolyte, several chemistries have been applied such as replacing Ge with other elements (Sn, Si) having compositions $Li_{10}SnP_2S_{12}$[15], $Li_{11}Si_2PS_{12}$[16], $Li_{10}Si_{0.3}Sn_{0.7}P_2S_{12}$[17]. However, the substitution of Ge with Sn, Si could not solve the issue of instability with Li-metal due to reduction M^{+4} ions to M^0 (M= Ge, Sn, Si)[18]. In the search for a more stable solid electrolyte having LGPS type structure, Kanno's group[19] has reported a composition $Li_{9.6}P_3S_{12}$ (i.e. $Li_{3.2}PS_4$) by considering mixed oxidation state (+4.8) of phosphorous (P) instead of +5. The $Li_{3.2}PS_4$ has shown better stability with Li-metal and high coulombic efficiency as compared to $Li_{10}GeP_2S_{12}$ electrolyte. To further improve the $Li_{3.2}PS_4$ electrolyte, partial substitution of S with O is also performed in $Li_{3.2}PS_{3.7}O_{0.3}$[12] with ionic conductivity of ~1.2×10^{-4} S cm^{-1} at room temperature. The partial substitution of S with O helps in achieving LGPS phase with higher purity.

Furthermore, halogen elements in LGPS structure were also incorporated to improve the ionic conductivity, and compound $Li_{9.54}Si_{1.74}P_{1.44}S_{11.7}Cl_{0.3}$ has shown the highest ion conductivity upto 2.5×10^{-2} S cm^{-1} at room temperature[19,20]. Recently, halogen atoms (Br, I) were explored in Li-P-S system and reported $Li_{10}P_3S_{12}Br$ and $Li_{10.25}P_3S_{12.25}I_{0.75}$ compounds with better conductivity and stability with Li metal[21].

It is considered that halogen elements can play an important role in tuning the ionic conductivity of sulfide solid electrolytes due to their unique properties such as (i) negative monovalent halogen ions have weaker interaction with Li-ions as compared to divalent S and O resulting in faster Li-ion conduction, (ii) larger radius of halogen anions (Br, I) leads to longer ionic bond and higher polarizability which facilitates the Li-ions migration, (iii) larger ionic radius of Br and I can provide additional path for Li-ion diffusion[21,22]. By considering the reported benefits of halogen doping in solid electrolytes, and further exploring the $Li_{3.2}PS_{3.7}O_{0.3}$ (LPSO) compound, we have synthesized a series of solid electrolytes by incorporating halogen atoms (Li, Br, and I) in Li-P-S-O system with $Li_{3.2+y}PS_{3.7}O_{0.3}X_y$ (X = Cl, Br, I, y= 0.1, 0.2) composition.

EXPERIMENTAL SECTION

Materials synthesis

The $Li_{3.2+y}PS_{3.7}O_{0.3}X_y$ (X = Cl, Br, I, y = 0, 0.1, 0.2) compounds are synthesized using the precursors Li_2S (Alfa Aesar, 99.9%), P_2S_5 (Sigma Aldrich, 99%), P_2O_5 (Alfa Aesar, 99.99%), P_{red} (Sigma Aldrich, 99.99%), LiCl (Sigma Aldrich, >99%), LiBr (Sigma Aldrich, 99.99%), and LiI (Sigma Aldrich, 99.95%) using mechanochemical method. The synthesis process is motivated by the previously reported papers[12,19]. The whole synthesis process is performed inside the glove box filled with high purity argon gas having moisture/H_2O and O_2 levels less than 0.1 ppm. Initially, all precursors were weighted according to stoichiometry, and the total precursor of 2.5 g was transferred to a ZrO_2 jar of 20 ml for ball milling using ZrO_2 balls of diameter 10 mm. The total ball milling of 135h was carried out by planetary milling Fritsch Pulverisette 7 at the speed of 500 RPM. However, effective ball milling time was 45h as the program used with 5 min running and 10 min pause. The milling process was stopped after every 22.5h of total ball milling (i.e. 7.5h of effective ball milling) and ZrO_2 jar was carried inside the glove box for scratching the material from the jar's wall. The scratched material was ground in a mortar pestle for 10 min and XRD data was collected each time to observe the intermediate changes before starting the next cycle of ball milling. A similar process was repeated multiple times to perform a total of 45h (7.5h×6) of effective ball milling. After 45h of effective ball milling, the prepared amorphous powder materials were pressed into pellets inside the glove box using 1 ton of pressure. These pellets were vacuum sealed inside the carbon coated quartz tube and calcined at 220 °C for 4 h at the heating rate of 100 °C/h. The calcination temperature was selected based on DSC results. After cooling down to room temperature, the sealed tube was carried inside a glove box and annealed pellets were ground in a mortar pestle to get the final crystalline powder.

Materials Characterization

The XRD measurement of $Li_{3.2+y}PS_{3.7}O_{0.3}X_y$ (X = Cl, Br, I, y = 0, 0.1, 0.2) compositions were carried by Rigaku miniflex (Cu-$K_{\alpha1}$ = 1.5405 Å and Cu-$K_{\alpha2}$ = 1.5444 Å) using an air-sensitive sample holder in which Kapton film is always at 90° to the X-ray beam. The phase identification of prepared compounds was done by X'Pert High Score Plus combined with COD, PDF-2 and ISCD databases. For detailed structural analysis, Rietveld refinement was performed using FullProf software.

The thermal properties of precursors and crystalline materials of $Li_{3.3}PS_{3.7}O_{0.3}X_{0.1}$ (X = Cl, Br, I) and $Li_{3.2}PS_{3.7}O_{0.3}$ compounds were investigated from 30 °C to 450 °C by Differential scanning calorimetry (DSC) combined with thermogravimetric analysis (TGA) using Netzsch STA 449F3. The powder samples were kept inside the alumina crucible and heated under an argon atmosphere at the heating rate of 2 °C/min.

The density of the compacted pellets was measured before the conductivity test by geometric method. The density was determined by using the formula: $\rho = \frac{m}{V}$ where m is mass of pellet and V is volume of the pellet. The volume of the pellet was calculated using formula $V = (A \times h)\ or\ \pi r^2 h$ where, A, r and h are surface area, radius and thickness of the pellets, respectively. The relative density of $Li_{3.3}PS_{3.7}O_{0.3}Cl_{0.1}$, $Li_{3.3}PS_{3.7}O_{0.3}Br_{0.1}$, $Li_{3.3}PS_{3.7}O_{0.3}I_{0.1}$ and $Li_{3.2}PS_{3.7}O_{0.3}$ compounds was found 94.0%, 94.0%, 94.5% and 94.5%, respectively if compared with density of $Li_{3.2}PS_4$ (1.85 g cm^{-3}).

The ionic conductivity of newly synthesis materials $Li_{3.3}PS_{3.7}O_{0.3}X_{0.1}$ (X = Cl, Br, I) and $Li_{3.2}PS_{3.7}O_{0.3}$ was determined by electrochemical impedance spectroscopy using BioLogic VMP3 analyzer in the frequency range from 1.0 MHz to 0.1 Hz with an amplitude of 50 mV. For the EIS measurement, first, 200 mg of solid electrolyte powder was pressed into a pellet of 10 mm diameter inside the glove box by applying a pressure of 188 MPa. Then, the pellet was vacuum-sealed inside the plastic bag and further compacted by isostatic pressure of 9.0 tons. Both sides of the compacted pellet were gold-coated to prepare blocking cells (Au/SE/Au). The pellet sample was placed inside the Controlled Environment Sample Holder (CESH) and the sample holder was put inside the Intermediate Temperature System (ITS) for conductivity measurement in the range of -40 °C to 80 °C. The samples were placed in the holder inside an argon gas-filled glove box to avoid any trace amount of oxygen and moisture inside the holder.

Furthermore, the room temperature ionic conductivity of all samples was also measured at 25 °C directly inside the battery cell (steel/SE/steel) used for the electrochemical study. For that, 40 mg of solid electrolyte powder was kept inside the battery cell of 7 mm diameter and pressed at the pressure of 255 MPa. The constant pressure was maintained during the measurement by screws of the cell.

The measured impedance spectra (Nyquist plots) recorded at -40 °C were fitted to an appropriate electrical equivalent circuit $[(R \| Q_1)+Q_2]$ for all samples by least squares method using Z-fit Ec-Lab software. However, total resistance (R) at room temperature was determined from the intersection of the spike and Z-axis of Nyquist plots. The total conductivity was calculated from resistance R and geometry of the pellets by using the formula $\sigma = \frac{l}{R \times A}$; where, R is total resistance, and l and A are the thickness and area of the pellet, respectively[23].

The electrochemical measurement of $Li_{3.3}PS_{3.7}O_{0.3}X_{0.1}$ (X = Cl, Br, I) and $Li_{3.2}PS_{3.7}O_{0.3}$ compounds was carried out in symmetric cell (Li/SE/Li) configuration at different current rates. In the critical current density (CCD) test program, the SSB cells were left in the rest for 5h at OCV to stabilize the solid interface between lithium metal and solid electrolytes, and a constant current was applied for 30 min at each step before increasing the current. The current was continuously increased till short circuits in the cells due to lithium dendrites formation.

Electrochemical study of full solid state battery in (NCA+SE)/SE/(graphite+SE) cell configuration using $LiNi_{0.8}Co_{0.15}Al_{0.05}O_2$ (NCA) as a cathode and graphite as anode by BioLogic VMP3 analyzer. Both cathode and anode materials were mixed with solid electrolyte (SE) in the ratio of 70:30 (NCA: SE) and 66:34 (graphite: SE) to ensure good contact among electrodes and electrolyte materials. For the SSB cell fabrication, about 40 mg of solid electrolyte (SE) powder was pressed inside the battery cell with 255 MPa of pressure for 1 min. Thereafter, about 8.5 mg mixture of graphite and SE was put over the surface of pressed electrolyte and again pressed with 255 MPa for 1 min. Similarly, about 8 mg mixture of NCA and SE was put over the other surface of the solid electrolyte, and a similar pressure was applied. In the end, all screws of the cell were tightened to maintain the constant pressure on the SSB cell during measurement. The galvanostatic charge-discharge cycles were recorded by using Biologic system at the current rate of C/10 (1C = 278.94 mA g^{-1}) which corresponds to about 0.39 mA cm^{-2}.

For the symmetric cell fabrication, about 50 mg of SE powder was pressed inside the battery cell at a pressure of 255 MPa for 1 min. Thereafter, thin layers of Li-metal were placed over both sides of solid electrolyte for making cell configuration as Li/SE/Li and battery cell tightened to provide adequate pressure during cycling.

Microstructures of prepared powders and pellets were determined by scanning electron microscopy (ZEISS Supra55 FEG). The microstructures of the pellets were recorded after EIS study and pellets were cut in half to record images from cross-sectional area.

The amount of H_2S generated from the prepared solid electrolyte samples was measured with a H_2S sensor (Croncow, Gasman) by exposing samples in ambient atmosphere for two hours. For the H_2S measurement, about 40±5 mg of solid electrolyte powder was pelletized in a 6 mm diameter die at the pressure of 255 MPa and placed inside a 4000 cm^3 air-tight vessel. In order to ensure a constant humidity level, 20 mL of H_2O was also placed inside the desiccator. The generated gas was recorded in ppm which was converted to cm^3/g according to the weight of the sample.

RESULTS AND DISCUSSION

In the present work, we have tried to explore the various possibilities to find out new compositions with LGPS-type structure having least impurity/secondary phases in the targeted LGPS-structured chemical composition $Li_{3.2+y}PS_{3.7}O_{0.3}X_y$ (X = Cl, Br, I and y = 0, 0.1, 0.2). We started the study with a small amount of single-element doping in the $Li_{3.2}PS_{3.7}O_{0.3}$ phase which further extended for multi-elements and higher content of halogen. The XRD patterns of all prepared samples according to $Li_{3.2+y}PS_{3.7}O_{0.3}X_y$ (X = Cl, Br, I and y = 0, 0.1, 0.2) composition are given in Figure 1(a). It can be seen that samples doped with a small amount of single element show maximum purity and adapting LGPS type structure which were indexed with ICSD (# 30161) and space group $P4_2/nmc$ using reference from published work[12,19,21,23]. However, apart from the Li_2S secondary phase that is always observed in LPSO compounds[12], halogen doped samples also show some additional peaks. However, intensity of Li_2S peak at 31.0° decreases with Cl and Br doping and completely vanished in LPSOI sample.

One additional unidentified XRD peak at 24.45° and 25.2° was observed for $Li_{3.3}PS_{3.7}O_{0.3}Cl_{0.1}$ and $Li_{3.3}PS_{3.7}O_{0.3}Br_{0.1}$ samples, respectively. In addition, sample $Li_{3.3}PS_{3.7}O_{0.3}I_{0.1}$ shows impurity peaks at 25.0°, 29.3°, 43.9°, 46.8° and 51.2° which are identified close to iodine (I_2) phase according to ICSD database (Ref. # 01-079-2355). When, we tried to preform refinement by including iodine phase, refinement did not improve. Therefore, we could not reach on the conclusion of this phase. We also tried doping two halogen elements together (Br and I, y = 0.1), (Br and I, y = 0.2) (Cl and Br, y = 0.2), and Br with higher concentration (y = 0.2). In all cases, purity of LGPS phase decreases and other impurity/secondary phases increase. Therefore, four samples with higher purity $Li_{3.2}PS_{3.7}O_{0.3}$ and $Li_{3.3}PS_{3.7}O_{0.3}Cl_{0.1}$, $Li_{3.3}PS_{3.7}O_{0.3}Br_{0.1}$, and $Li_{3.3}PS_{3.7}O_{0.3}I_{0.1}$ were selected for the further study and samples were designated as LSPO, LPSOCl, LPSOBr and LPSOI, respectively. These compounds have some impurity phases, therefore, actual composition may be different than nominal composition. Since, quantification of impurity phases was not done in present study, therefore, for the simplicity, nominal compositions are used throughout the paper.

For the detailed analysis, Le Bail refinement analysis was performed on selected samples as shown in Figure 1(b). The refinement results suggest that all compounds have adopted the LGPS-type structure with some impurity peaks in LPSOI which needs further detailed investigation. However, we have succeeded in performing Rietveld refinement analysis on LPSO sample using initial parameters from literature[12,19], and the refinement graph and the results are given in Figure S1 and table S2 of Supporting Information. The atomic positions, occupancy of Li and thermal parameters of all atoms were fixed during the refinement. The refinement results suggest about 3.5 wt.% of Li_2S as secondary/impurity phase which is also present in halogen doped samples. Therefore, 3.5 wt.% of Li_2S secondary phase is assumed in all samples. The lattice parameters and cell volume increase with doping of Br and I in the LPSO compound, whereas, opposite results were found for Cl doped sample as shown in Figure 1(c). The increment/decrement in lattice parameters and cell volume of halogen doped compounds is due to the difference of ionic radii of doped elements (Cl, Br, I) from S and O atoms. The order of ionic radii (Å) of anions is O^{2-} (1.35) < Cl^{-} (1.81) < S^{2-} (1.84) < Br^{-} (1.96) < I^{-} (2.20)[24] which is consistent with the order of changes in lattice parameters and cell volumes of samples i.e. LPSOCl < LPSO < LPSOBr < LPSOI. The change in the cell volumes of LPSO and LPSOCl is smaller as compared to LPSOBr and LPSOI which could be due to a very small difference in ionic radii of Cl^{-} (1.81) and S^{2-} (1.84). According to these results, it can be assumed that halogen atoms occupy the position of S atoms in the structure. However, another study has reported new sites of Br and I in the LGPS type structure[21]. A detailed structural analysis is being carried out by transmission electron microscopy/neutron diffraction to find out the impurity peaks and positions of halogen in LPSO compound. The work purely based on structural analysis will be published in separate study in future.

The calcination temperature of precursors after ball milling was selected based on the DSC results of precursors as shown in Figure 1(d). All compounds show major exothermic peaks in the range of 210 °C to 230 °C. Therefore, the calcination temperature for all compounds was selected at 220 °C. The compounds $Li_{3.3}PS_{3.7}O_{0.3}Br_{0.1}$ and $Li_{3.2}PS_{3.7}O_{0.3}$ show two exothermic peaks whereas $Li_{3.3}PS_{3.7}O_{0.3}X_{0.1}$ (X = Cl, I) show only one peaks. The stability of the compounds was also checked by DCS measurement and results are shown in Figure 1(e). The broad endothermic peaks are observed for all compounds near 100 °C which could be due to moisture absorbance on the powder surface. Thereafter, no activity was noticed up to 315 °C which shows the stability of the compounds over this temperature range. However, a major reactivity was noticed after 315 °C in all compounds due to decomposition of materials. To find out the decomposition compounds, samples LPSO and LPSOBr were calcined at 350 °C in a quartz tube using similar conditions. The XRD results show β-Li_3PS_4 is a major phase in both samples and results are shown in Supporting Information (Figure S3). Similar β-Li_3PS_4 phase was obtained in previous study also[21].

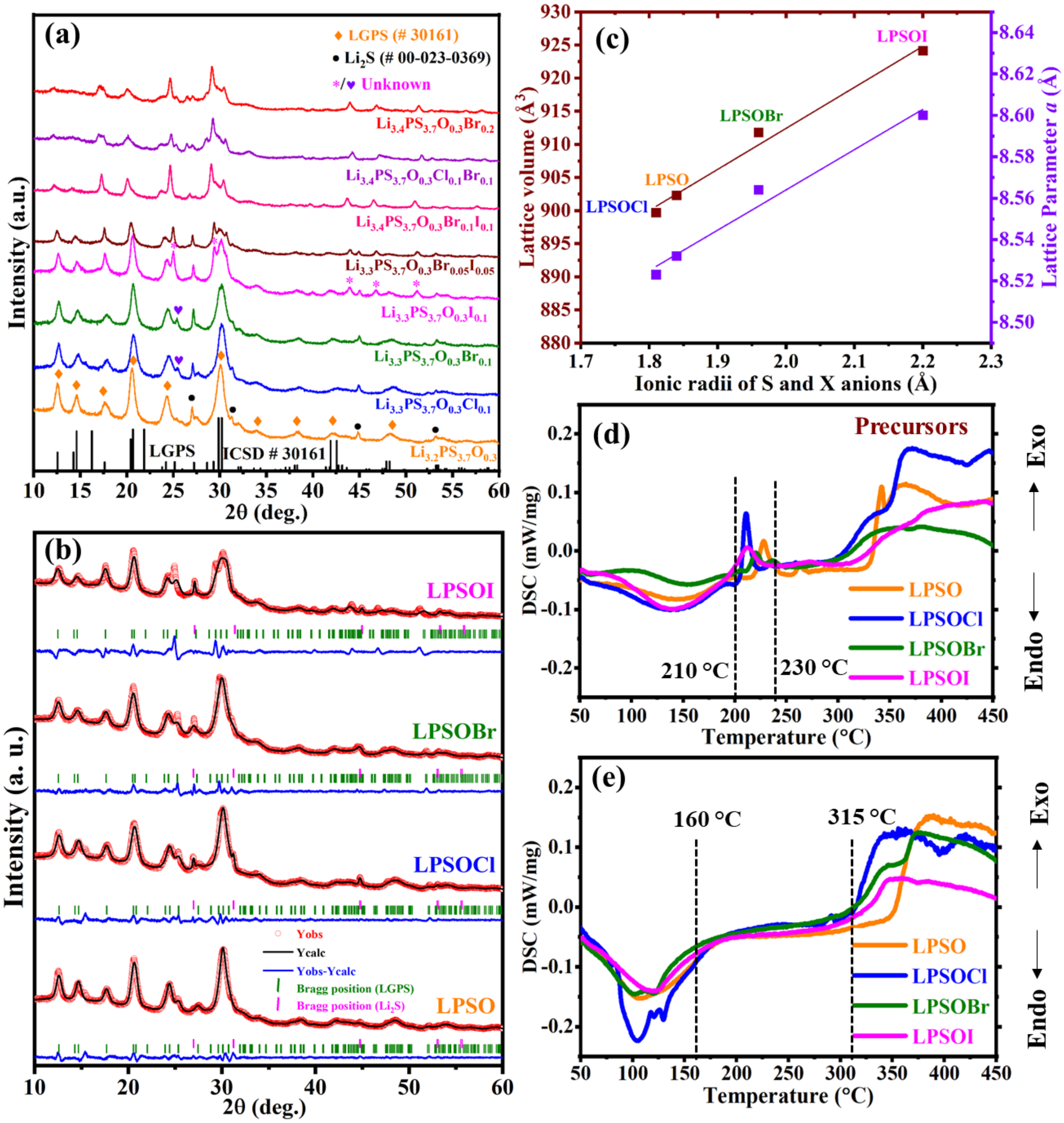

Figure 1. (a) XRD patterns of $Li_{3.3}PS_{3.7}O_{0.3}X_{0.1}$ (X = Cl, Br, I) and $Li_{3.2}PS_{3.7}O_{0.3}$ compounds, (b) Le Bail Rietveld refinement graphs, (c) change in lattice parameters and cell volume with halogen, and (d) DSC results of precursors after ball milling, (e) DSC results of prepared compounds to show stability temperature range.

The density of the compacted pellets is given in table 1 which was measured before the conductivity test by geometric method as explained in experimental section. The AC impedance measurement was performed to determine the electrical conductivity of the prepared electrolytes in the form of compacted pellets. Figures 2(a) and 2(b) show Nyquist plots at 25 °C and -40 °C, respectively of cells in Au/SE/Au geometry. It can be seen from the Nyquist plots recorded at 25 °C, the samples do not show proper semicircles due to the low impedance, similar pheneomenon has been reported earlier also[10,25]. Therefore, the total resistance of the samples was determined by intersection of spike and Z-axis. The LPSOI and LPSOBr samples show lower resistance as compared to LPSO, whereas, LPSOCl sample shows highest resistance. It means that Cl doping is not beneficial for the conductivity improvement of LPSO electrolytes. Whereas, Br and I doping show a positive impact on conductivity of the LSPO compound. When the EIS data was recorded at lower than room temperature, a semicircle started to appear and a proper semicircle was observed at -40 °C due to the slow kinetics of Li ions at low temperatures[17]. The resistance at -40 °C was calculated by Z-fitting using an electrical equivalent circuit $[(R\|Q_1)+Q_2]$. Where R is resistance related to solid electrolyte (SE) which is combination of grain/bulk resistance and grain boundary resistance. The Q_1 is used for capacitive behavior of non-ideal capacitor or called constant phase element. The non-ideal capacitive behavior of constant phase element is not fully understood but it generally assigned to inhomogeneity, surface roughness, porosity and tortuosity of materials[26,27]. The spike in the low frequency region appears due to charge build-up at the blocking electrodes (Au in this case)[28] and represented by constant phase element Q_2 (also denoted by Z_{CPE}). The Z_{CPE} can be calculated by the relation: $Z_{CPE} = Q^{-1} * (i\omega)^{-n}$, where $n \leq 1$, and corresponding capacitance can be estimated by $C = [R^{1-n} * Q]^{1/n}$ [17,29]. The capacitance of semicircle can be calculated by relation ($\omega_{max} = R \times C$),where $\omega_{max}(\frac{1}{2\pi f})$ is angular frequency at the maxima of semicircle and R is resistance of semicircle[17]. It is generally found in sulfide electrolyte that due to high conductivity, ductile nature and better compaction, signal response from grains and gain boundaries overlaps causing resistances of gain and grain boundary hard to distinguish[27,30]. In our case also, we got only one semicircle even at low temperature (-40 °C) whereas some of the studies could able to distinguish grain and grain boundary resistance at low temperature[12,30]. The sample LPSOI shows the highest conductivity of 0.55 mS cm^{-1} at 25 °C, whereas, LPSOCl shows the lowest value as given in Table 1. The activation energies (E_a) of the samples were calculated from linear extrapolation of the Arrhenius plot as shown in Figure 2(c). The lower E_a values of LPSOI and LPSOBr samples are consistent with conductivity values which means I and Br doping facilitate the ionic diffusion inside the structure. Lower activation energy implies that a lower potential energy barrier is required for ions to jump to adjacent lattice sites, resulting in more active lithium-ion jumps[31].

The conductivity and activation results also support the hypothesis that doping of larger anions may provide additional space inside the structure for lithium diffusion as ionic radii of I and Br are larger than S, similar results are also found earlier[21], whereas, we have observed opposite results in the case of Cl doping.

We have further measured the conductivity at 25 °C directly using the battery cell in steel/SE/steel configuration at the constant pressure of 255 MPa to co-relate the performance of solid state battery with conductivity of the solid electrolytes. and the results are shown in Figure 2(d). The conductivity of the samples follows a similar trend as observed for pelletized samples (Figure 2a). The maximum conductivity of 0.93(≈ 1.0) mS cm^{-1} was obtained for the LPSOI sample, whereas, LSPOCl shows the lowest value. The total resistance (bulk + grain boundary) and conductivity (ionic + electronic) of all samples are given in table 1. The conductivities of all samples in steel/SE/steel configuration were found higher than Au/SE/Au cell because of lower interfacial/contact resistance due to applied pressure. In the steel/SE/steel cell, a continuous pressure of 255 MPa was applied during the measurement which provided better contact between solid electrolyte and current collectors. This means the conductivity of the material also depends on the measurement method and applied pressure[32]. We have also measured the conductivity for other samples with less purity in the steel/SE/steel configuration and the results are given in Supporting Information (Figure S4 and Table S5).

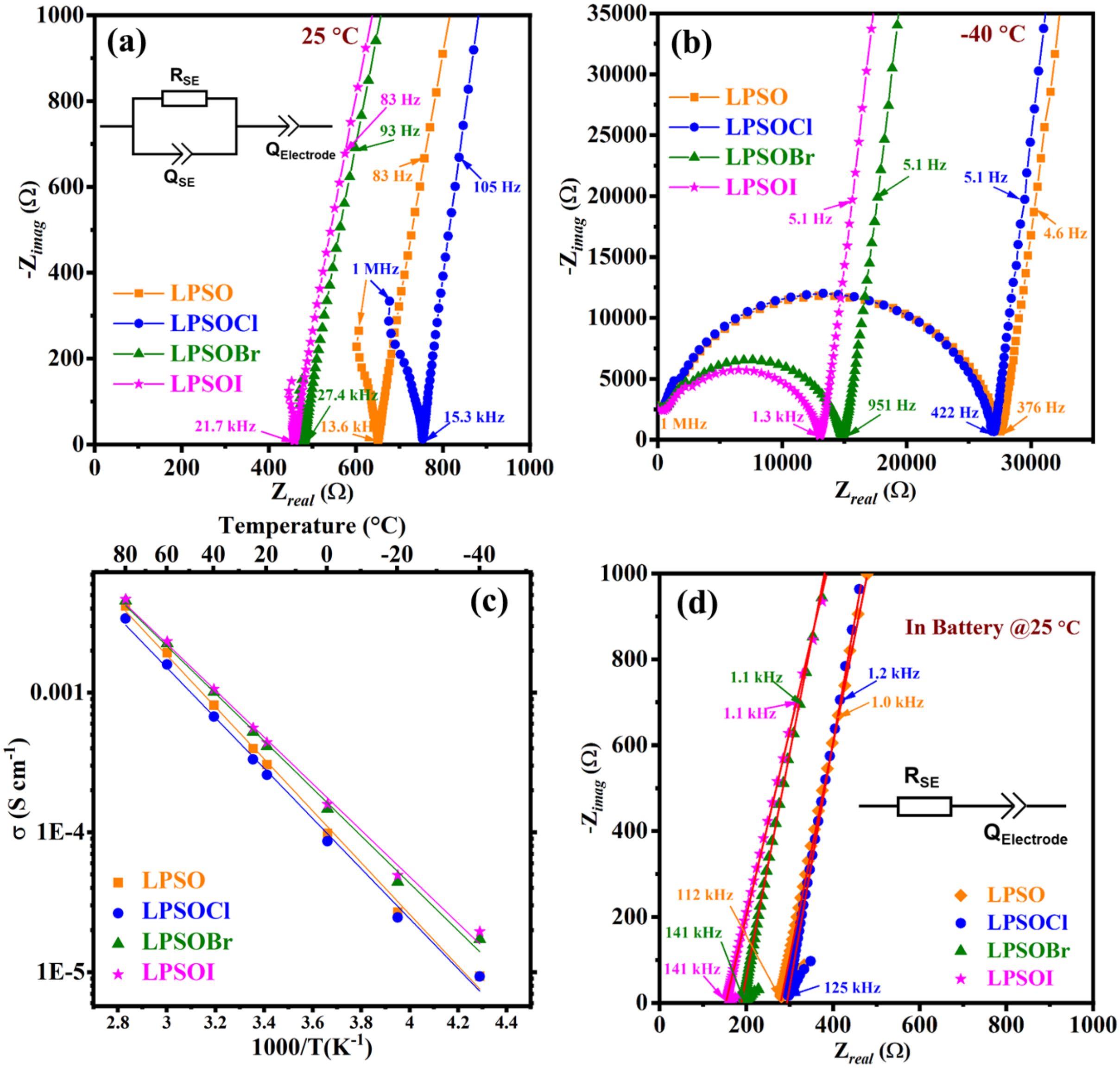

Figure 2. Nyquist plots recorded in Au/SE/Au cell at (a) 25 °C, (b) -40 °C, (c) Arrhenius conductivity plots in between -40 °C to 80 °C, and (d) Nyquist plots recorded in steel/SE/steel cell at 25 °C.

Table 1. EIS results and relative density of solid electrolytes recorded at 25 °C.

Sample	**Abbr.**	**Results in Au/SE/Au cell**				**Results in steel/SE/steel cell**		
		R_{Total} (Ω)	σ (mS cm^{-1})	E_a (eV)	$\rho_{Rel.}$ (%)	R_{Total} (Ω)	σ (mS cm^{-1})	$\rho_{Rel.}$ (%)
$Li_{3.2}PS_{3.7}O_{0.3}$	LPSO	650	0.39	0.37	94.0	272	0.5	94
$Li_{3.3}PS_{3.7}O_{0.3}Cl_{0.1}$	LPSOCl	753	0.33	0.36	94.0	295	0.45	94
$Li_{3.3}PS_{3.7}O_{0.3}Br_{0.1}$	LPSOBr	480	0.53	0.34	94.5	195	0.77	94
$Li_{3.3}PS_{3.7}O_{0.3}I_{0.1}$	LPSOI	459	0.55	0.33	94.5	152	0.93	94

The microstructures of prepared powder samples and pelletized samples (after the EIS Test) were determined by SEM analysis and results are shown in Figure 3. The powder samples show a large range of particle size starting from less than 1 µm to 10 µm, even some particles look more than 10 µm as shown in Figure 3(a-d). However, if we look closer view of bigger particles in the magnified images given in the inset, it seems that bigger particles were formed by the agglomeration of small particles. Therefore, the actual particle size might be lower than that observed in the images.

The microstructures of pellets show highly dense microstructure that can be linked to more than 94% of relative density of all pellets. Therefore, highly dense pellets can be achieved from halogen-doped solid electrolytes by cold pressing. However, microstructures show some micro cracks. These cracks might be formed during EIS measurement when pellets were heated up to 80 °C and cooled down to -40 °C. The morphologies of halogen doped samples are found different (e.g. cuboid) in pellet form as compared to powder. Furthermore, the pellet sample of LPSOI shows morphology like French fries in Figure 3(h) whereas the powder sample did not. To verify the composition of the French fries' morphology whether it is a new phase or LPSOI, SEM-EDS compositional analysis was carried out and results are given in Supporting Information (Figure S6). The EDS results show a similar composition as LSPOI which means a change in morphology will have occurred during either pelletizing the powder or EIS measurement. To find the origin of morphology change, a pellet of LPSOI was prepared in a similar way, and SEM and elemental compositional analysis was performed before EIS measurement. The microstructure of the pellet (cross-sectional view) is shown in Figure S7(a-b) of Supporting Information. The microstructure of the LPSOI layer in full SSB was also measured before charge-discharge cycling as shown in Figure S7(e) of Supporting Information. In both cases, the morphology of the LPSOI was observed like French fries. Therefore, the morphology of LPSOI is changed due to applied pressure in anyways either unidirectional or isostatic. The elemental compositional analysis of LPSOI pellet before EIS also confirm similar composition of both French fries and bulk shaped samples as shown in Supporting Information (Figure S7). To further confirm the phase, XRD was conducted on pellets of LPSOI and results shows similar as powder samples.

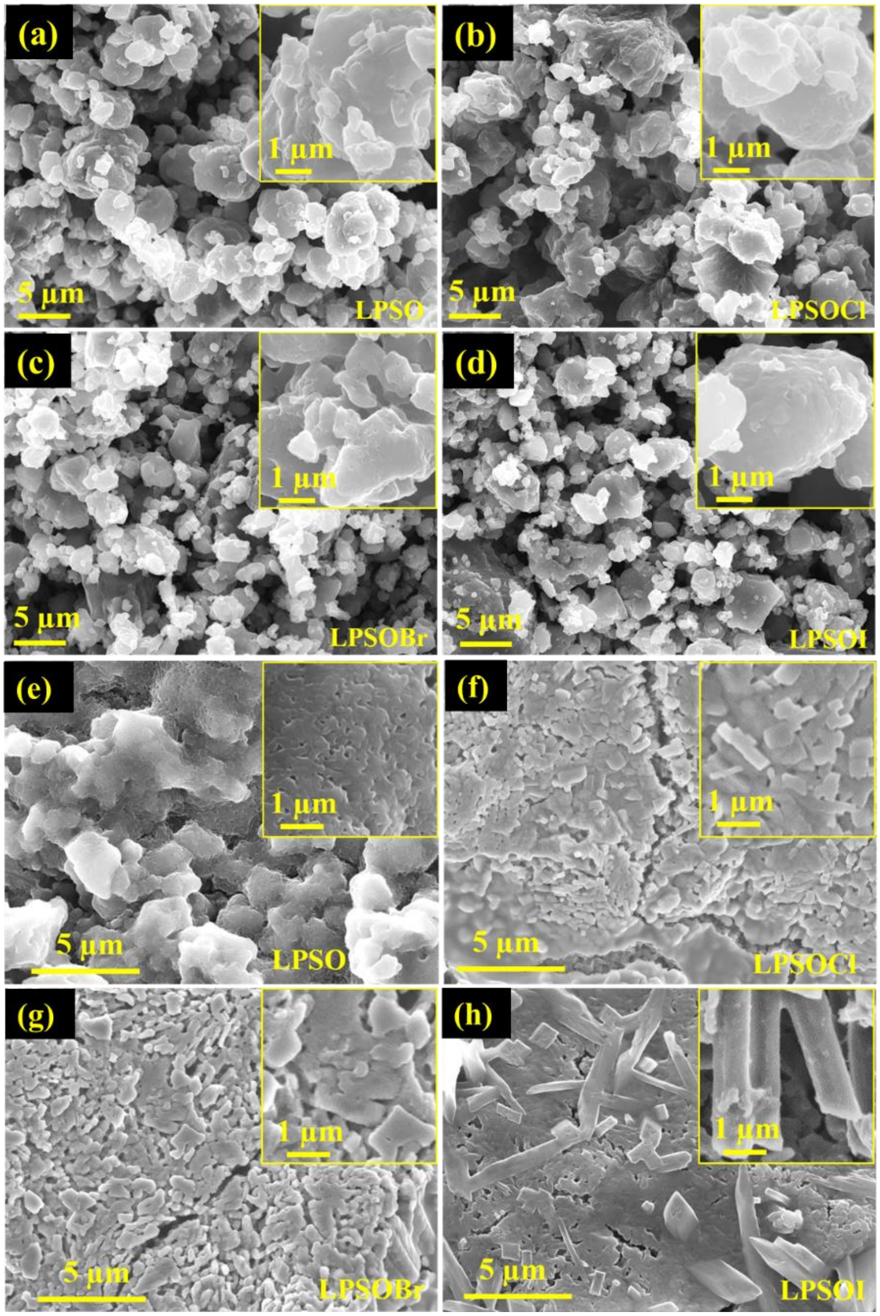

Figure 3. (a-d) Microstructure of powder samples, and (e-f) microstructure of pellet samples.

The CV measurement of Li/SE/Au cell was recorded in the potential range of 0-5V at the scan rate of 0.1 mV s^{-1} and results are shown in Figure 4(a). The CV results show excellent electrochemical stability of the electrolytes up to 5V and no redox peaks are observed throughout the range except between 0 to 0.6V. The cathodic peaks observed between 0 to 0.2V (before the dotted line) are due to lithium deposition on the Au electrode and forming Li-Au alloy[33,34]. The three anodic peaks are also noticed in the potential range of 0.2-0.6V due to the de-alloying or dissolution of lithium from the Au electrode through the following reactions: Li_3Au to Li_5Au_3, Li_5Au_3 to Li_3Au_2, and Li_3Au_2 to Li_3Au_5[35–37]. From the intensities of anodic and cathodic peaks, it can be hypothesized that halogen-doped samples show more stability than LSPO during Li-alloying/ de-alloying. The intensities of anodic and cathodic peaks are lowest for LPSOI which supports the stability of the sample.

The final goal of solid-state batteries is to use lithium metal as an anode, therefore, the stability of prepared solid electrolytes against lithium metal was determined by polarization vs. time profiles in symmetric cells (Li/SE/Li) as shown in Figure 4(b-e). First, a critical current density (CCD) test of solid electrolyte was performed which defines the power density of batteries as shown in Figure 4(b). The CCD test helps to understand the interfacial reactivity between solid electrolytes and lithium metal, dendrites formation, and maximum acceptable current for solid electrolytes before a short circuit or battery failure[38]. It can be seen that LPSOI electrolyte bore a maximum current of 0.80 mA cm^{-2} before failure, whereas, LPSOCl could tolerate only up to 0.60 mA cm^{-2} with high polarization due to soft short circuit[38]. The current bearing capacity of LPSOBr and LPSO was observed 0.65 mA cm^{-2} and 0.70 mA $cm^{-2,}$ respectively. The CCD results suggest that the high conductivity of LPSOI sample helps in smooth lithium diffusion which allows it to bear the maximum current density and also slows down dendrite formation[21,33,34].

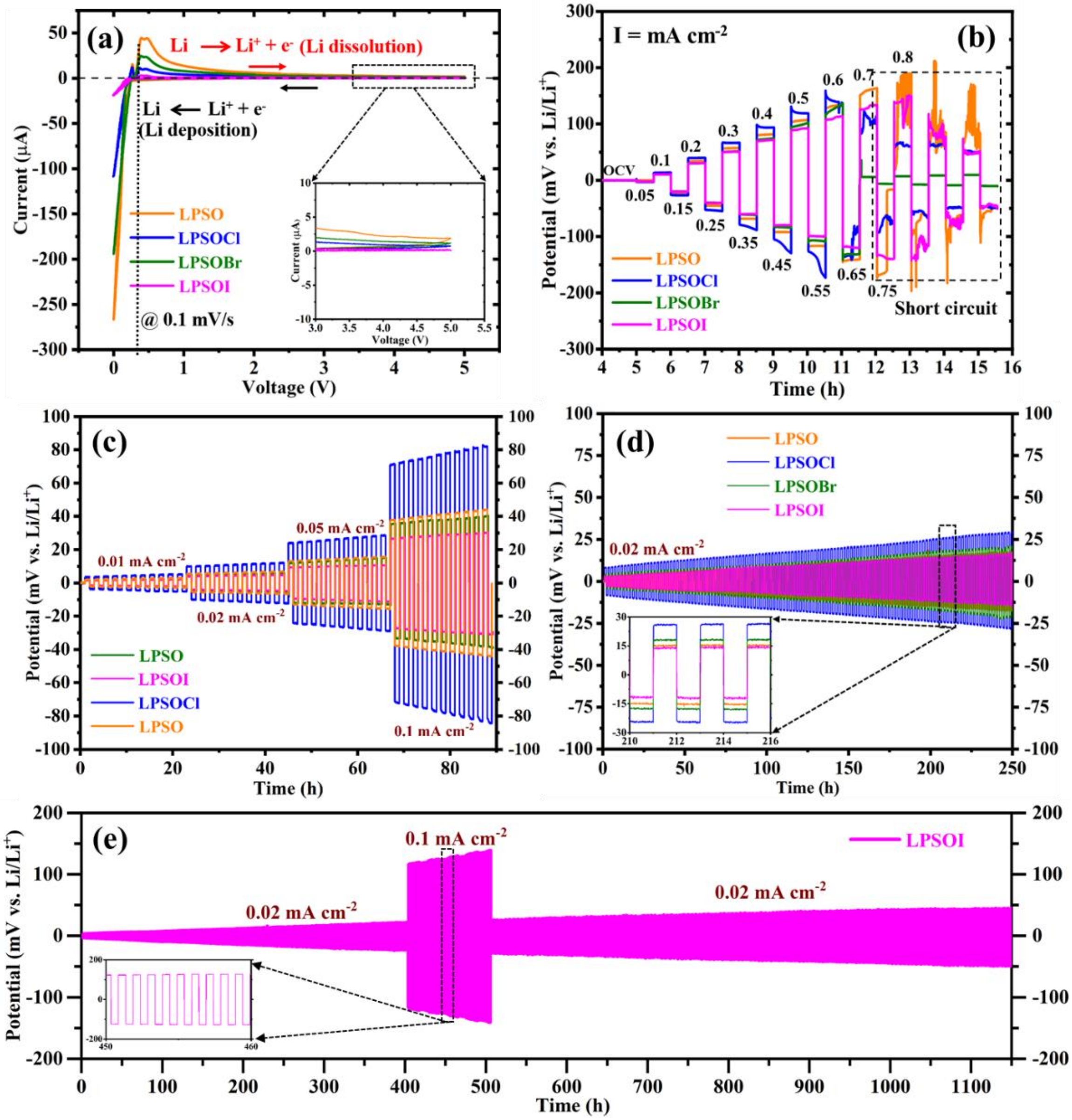

Figure 4. Electrochemical results of all samples in symmetric cells (Li/SE/Li), (a) CV curves of Li/SE/Au cells at a scan rate of 1 mV s^{-1} between 0 - 5 V (vs. Li/Li$^+$), inset graph shows no side reaction at high potential, (b) Critical current density (CCD) graphs, (c) Polarization profiles at different current rates, (d) Comparison of polarization profiles, and (e) Polarization profiles of LPSOI showing long cyclability against lithium metal.

We further tested critical current density with longer time in Figure 4(c) which also shows lower polarization and better stability of Br and I doped LSPO samples. Figure 4(d) shows the interfacial stability of prepared solid electrolytes with lithium metal in terms of polarization up to 250 h and these results also validate better stability of LPSOI and LPSOBr samples with lower polarization. The LPSOI solid electrolyte shows best stability among all samples, therefore, it further was tested for very long time of 1150 h, and the cell worked smoothly without any short circuit as shown in Figure 4(e).

After proving the stability of solid electrolytes against lithium metal, full solid-state batteries (SSBs) were prepared in the (NCA: SE, 70:30)/SE/(graphite: SE, 70:30) cell configuration, and the details of SSBs fabrication are given in experimental section. The galvanostatic charge-discharge cycles were recorded at a current rate of C/10 rate (1C = 278.94 mA g^{-1}) calculated according to the weight of active material in the composite cathode and results are shown in Figures 5(a-c). The first charge capacities of LPSO, LPSOCl, LPSOBr and LPSOI are 162 mAh g^{-1}, 182 mAh g^{-1}, 182 mAh g^{-1}, and 179 mAh g^{-1}, whereas, discharge capacities are 110 mAh g^{-1}, 124 mAh g^{-1}, 129 mAh g^{-1}, and 126 mAh g^{-1}, respectively. The large irreversible capacity noticed for all samples could be due to lithium consumption in the interfacial reactions to form solid electrolyte interface (SEI)[19,39]. The capacity loss during the first cycle for the samples LPSO, LPSOCl, LPSOBr, and LPSOI is 32%, 32%, 29%, and 29%, respectively. Sample LPSO shows the lowest charge and discharge capacities, but the capacity loss is equal for LPSO and LPSOCl samples. Whereas, LPSOI and LPSOBr not only show minimum capacity loss but also higher charge-discharge capacities due to superior conductivity of the materials. Figure 5(b) shows the charge-discharge capacities of the second cycle and a very small difference was noticed in charge-discharge capacities. From the second cycle, the coulombic efficiency was found quite stable (about 95%) up to 20 cycles which means a very stable SEI formed during the first cycle as shown in Figure 5(c). However, a continuous capacity loss is noticed for all samples and reached near 50% except LSPOI which shows a loss of only 40%. The stable cycle life in SSBs is still a challenge and very limited literature is available on long cycling life. The capacity loss may depend on many factors such as the selection of electrode materials, the ratio of cathode and anode materials, the thickness of the solid electrolyte layer, applied current, etc. One should be noticed that we have used non-coated NCA cathode which is more prone to react with sulfide solid electrolytes as compared to $LiNbO_3$-coated NCA[32,40] Therefore, a further detailed interfacial study is performed to know more about interfacial reactions as shown in Figure 6.

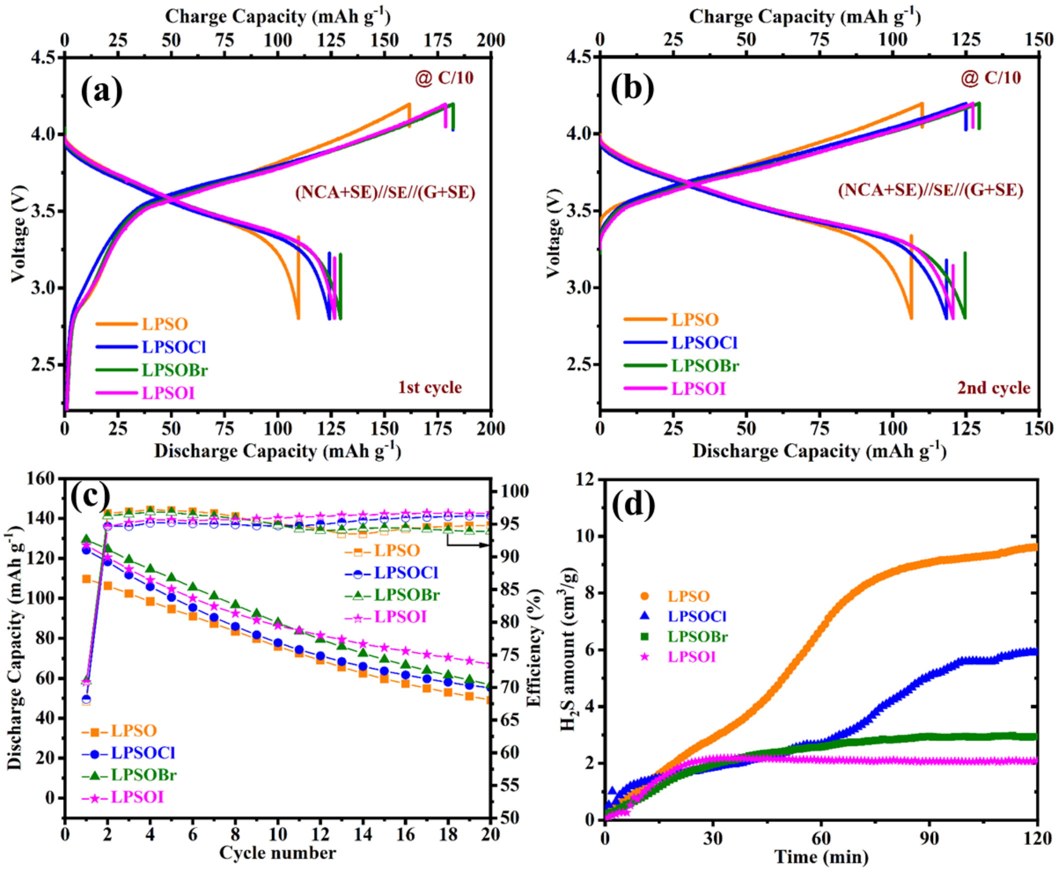

Figure 5. (a-c) Electrochemical performance of full SSB at current rate of 0.1C, (a) Charge-discharge curves of fist cycle, (b) Charge-discharge curves of second cycle, (c) Capacity retention

and coulombic efficiency up to 20 cycles of full SSBs, and (d) H_2S generated after exposing solid electrolyte samples into air and moisture.

The stability of sulfide-based solid electrolytes in ambient environments is very necessary for the safety and wide commercialization of these materials. Therefore, H_2S gas generated from the newly prepared solid electrolytes in ambient conditions is shown in Figure 5(d). It can be seen clearly from the graphs that halogen-doped samples are more stable as compared to LPSO. Furthermore, the samples LPSOBr and LPSOI are very stable which implies that Br and I doping not only increases the conductivity of LPSO but also improves stability in ambient environment.

For better understanding on stability and H_2S gas evaluation, we have compared our compounds with other reported compounds with LGPS structure, glassy Li_3PS_4, or thio-LISICON. Muramatsu et al. reported $75Li_2S \cdot 25P_2S_5$ glass-ceramic solid electrolyte which showed a conductivity of 1.9×10^{-4} S cm^{-1} at room temperature in argon atmosphere. The conductivity of the compound was reduced to 1.5×10^{-4} S cm^{-1} after air exposure[41]. Hayashi et al. tried to improve the chemical stability of Li_3PS_4 glass electrolyte by adding ZnO, Fe_2O_3, and Bi_2O_3. The composite electrolyte of $90Li_3PS_4$-10ZnO (mol%) showed ionic conductivity of 3×10^{-4} S cm^{-1} and better stability in air[8]. The conductivity (6.7×10^{-4} S cm^{-1}) of our LPSOI compound at room temperature is higher than both reported similar compounds. Tufail et al.[42] reported an air-induced degradation mechanism of $Li_7P_3S_{11}$ solid electrolyte. The compound showed the generation of H_2S about 2.7 $\times 10^{-2}$ cm^3 g^{-1} min^{-1} and continued to increase even after 50 min, whereas, our compound LPSOI did not show any H_2S generation after 30 min (as shown in Fig. 5d). Xu et al.[43] performed the H_2S gas evaluation study on the LGPS-type solid electrolytes M-$Li_9P_3S_9O_3$ and Q-$Li_9P_3S_9O_3$ prepared by mechanochemical and melt quench process, respectively. Samples M-$Li_9P_3S_9O_3$ and Q-$Li_9P_3S_9O_3$ have released about 0.8 wt.% and 0.3 wt.% H_2S gas on exposed to air for 6h. Audric et al.[44] also reported H_2S gas evolution of LGPS-type compounds $Li_3P_{1-x}B_xS_{4-x}$, and compared with Li_3BS_3, $\beta-Li_3PS_4$, and $Li_{10}GeP_2S_{12}$ after exposition to air versus time. The $Li_3P_{1-x}B_xS_{4-x}$ compounds show very high reactivity and H_2S gas value reached 30 $cm^3\ g^{-1}$ in just 5-10 min. In comparison to these studies, our LPSOI compound shows better stability. However, many studies have chosen different parameters and ways of experiment, and also selected different representation methods.

To understand the interfacial behaviors of prepared halogen doped solid electrolytes with NCA cathode and graphite anode in full solid state battery, *in-situ* EIS study was performed on the battery cells during charge-discharge cycling and results are shown in Figure 6. The nyquist plots of battery cells prepared with LOSOCl, LPSOBr and LPSOI are recorded for as prepared battery, and after 1st, 4th, and 10th charge-discharge cycle. The data interpretation/analysis was done using equivalent circuit mode by Z-fit software and possible understanding of the charge-discharge process inside the battery cells. During the charge-discharge process, following steps are involved and might be responsible for various interfacial reactions: (i) Li-ions diffusion and migration in solid electrolytes, (ii) diffusion of ions and electrons in active materials particles (e.g. NCA and graphite), (iii) migration of ions and electrons across composite cathode/anode thickness, (iv) migration of ions and electrons through solid electrolyte interface (SEI) or solid-solid interface, (v) double-layer formation at electrode/electrolyte interface, and (vi) transfer of electrons from current collector to cathode/anode composite[45]. However, multiple processes occurred in full cell are difficult to deconvolute from a single experimental spectrum due to overlapping of information[45,46]. The high frequency region is often disturbed by inductances, therefore, some of the data points in the high frequency region were removed for the reliable fitting. The similar perturbation in data at higher frequency also reported earlier[25].

The nyquist plots of as prepared full battery cells with LPSOCl, LPSOBr and LPSOI are shown in Figures 6 (a, e & i), respectively. The as prepared battery cells are in discharge stage (OCV = ~ 400 mV), in which graphite anode behave like a blocking electrode, therefore, impedance contribution would be only from solid electrolyte. The value of R_{SE} is total resistance due to solid electrolytes (bulk+ grain boundary) calculated from intersection between x-axis and spikes. In this case, equivalent circuit model $R_{SE}+Q_{Electrode}$ is used for fitting. The value of R_{SE} is increases on cycling from as prepared to 10th cycle for all three samples (shown by shaded area). Increasing R_{SE} values may be possible due to pressure modification or pressure relaxation during cycling causing higher grain boundary resistance. It is well know that the conductivity of sulfide based solid electrolytes varies with applied pressure[32]. The increment in R_{SE} values of LPSOI is lower as compared to LPSOBr and LPSOCl due to higher conductivity and better stability of the LPSOI solid electrolyte. Whereas, sample LPSOCl shows highest R_{SE} resistance, even though, an incomplete semicircle in high frequency region start appearing after fist cycle which further grows upto 10th cycle due to increasing impedance from grain and grain boundaries of LPSOCl. The first incomplete semicircles of LPSOCl in Figure 6 (b-d) show capacitance value in the range of 10^{-12} F which is associated to bulk resistance, however, it also has contribution of grain boundaries due to poorly resolved contribution of bulk and grain boundary separately[27]. The overlapping of bulk and grain boundary contribution is common due to high conducting grain boundaries of sulfide solid electrolytes[32,47].

However, depressed semicircles in mid frequency range having capacitance value in the order of 10^{-6} F are appeared for all three samples recorded after 1st ,4th and 10th cycle due to impedance contribution from solid-solid interface (SSI). The impedance of SSI is the sum of both anode and cathode composites. If we discuss about the values of R_{SSI} of LPSOBr and LPSOI, the full battery cell prepared with LPSOBr shows lower R_{SSI} values recorded after 1st and 4th cycle as compared to LPSOI. This could be possible due more stable interface between LPSOBr and NCA in the beginning as compared to LPSOI electrolyte which can also relate to higher initial capacity of LPSOBr battery cell as shown in Fig. 5 (a & b). However, interfacial resistance of LPSOI become almost constant from 4th to 10th cycle with minimal increment in R_{SSI} from 320 Ω to 323Ω, whereas, R_{SSI} of LPSOBr is increased from 282 Ω to 323Ω during the same interval. This characteristic can be understood by interlayer hypothesis formed by-products of NCA cathode, and LPSOI/LPSOBr electrolytes. The byproduct of LPSOI and NCA cathode formed a stable interlayer which prevents further reactivity of both materials leading to constant R_{SSI} whereas interface between LPSOBr and NCA continuously reacts due to unstable interlayer or contact loss within the cathode composites[48]. This phenomenon can also relate to cycling stability results shown in Fig. 5(c), even though LPSOBr battery shows initial higher capacity than LPSOI but after 10 cycles, capacity of LPSOI battery overpass and shows more stable capacity as compared to LPSOBr. However, R_{SSI} of LPSOCl battery is highest in all the samples due to higher reactivity with electrodes materials which is already found in lower capacity and cycle life of LPSOCl as shown in Figure 5. The schematic diagram of full solid state battery is shown in Figure 5(m) along with equivalent circuits used for different nyquist plots.

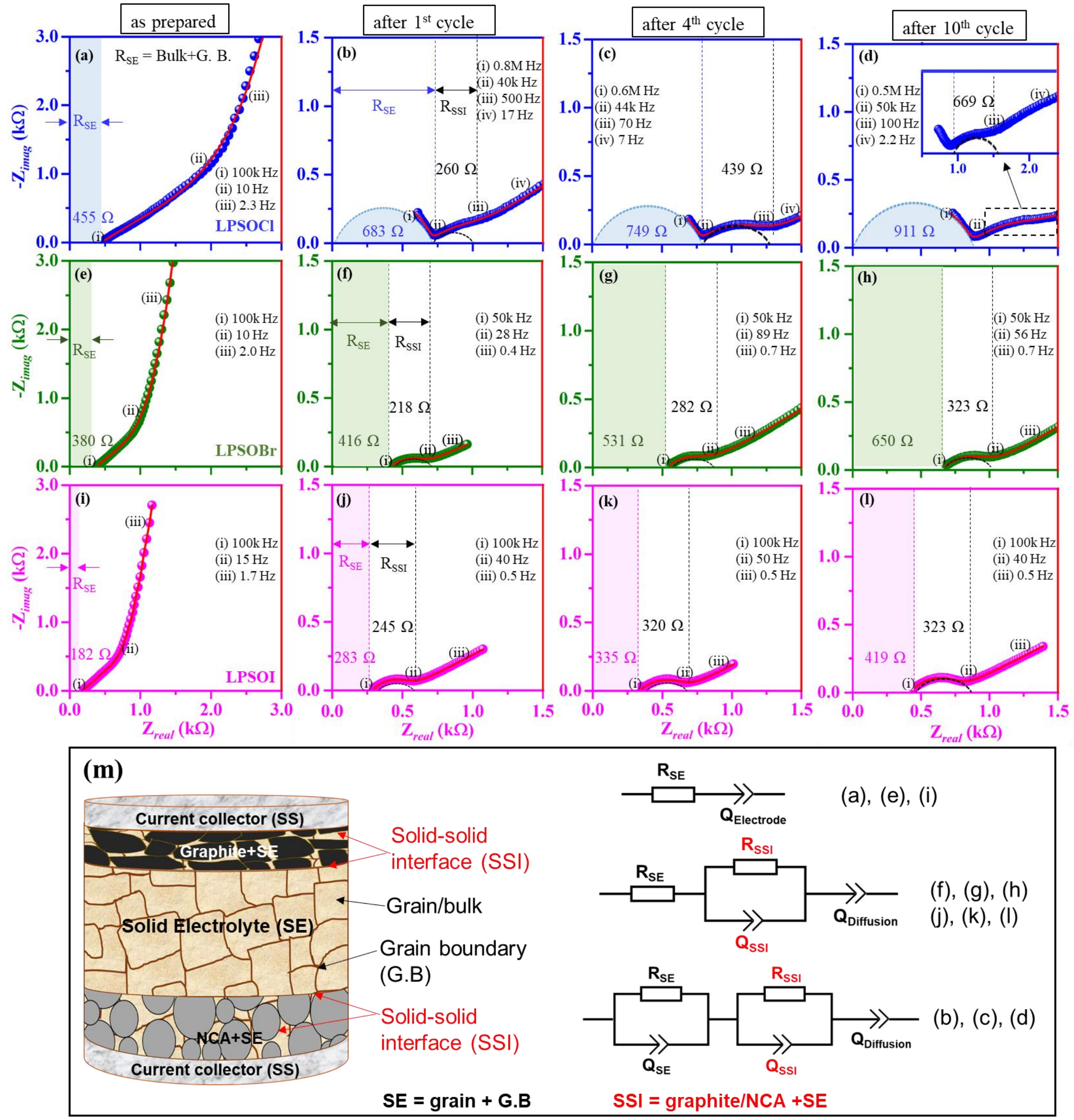

Figure 6. Nyquist plots recorded for as prepared, and after 1st, 4th, and 10th charge-discharge cycle of full solid state battery cell (NCA/SE/graphite) of (a-d) LPSOCl, (e-h) LPSOBr, (i-l) LPSOI; (m) Schematic diagram of full solid state battery cell and equivalent circuit used for fitting of different nyquist plots as mentioned in front of each circuit.

To observe the interfacial stability with Li-metal, full cells were prepared in similar way using Li-metal as anode instead of graphite as shown in Figure 7. In the battery cell prepared with Li-metal, impedance difference is too high between LPSOCl, LPSOBr and LPSOI, so we have used different scale for all three samples to see clear changes in impedance with cycling.

The nyquist plots of as prepared battery cells (shown in 7a, 7e & 7i) also show both SE and SSI contributions due to Li-metal (source of Li), and battery cells behave as it is already in charge stage (OCV= ~ 2.85V) which was not the case for graphite anode. The all three samples follow the similar trend as for the results shown in Figure 6. However, impedance is much higher in the cells with Li metal as compared to graphite anode due to reactivity of sulfide materials with Li metal[25,49]. Furthermore, stacking pressure was lower in the battery cells with Li metal to avoid the short circuit due to piercing of Li through electrolyte. Possibility of imperfect contact between solid electrolyte and Li metal cannot be neglected because stack pressure also influences the impedance values[32,50]. The value of R_{SS} and R_{SSI} are increased very rapidly from 1st to 10th cycle suggesting high interfacial reactions in solid electrolytes as well as both electrodes sides, respectively. Increasing R_{SS} value could be due to above mentioned reason of pressure relaxation. Particle size distribution also plays important role in reducing porosity of solid electrolyte which affect the impedance. Generally, hot pressing is used to improve the porosity[32], while, we have used cold pressing only, therefore, low compaction could also be the reason for increasing R_{SS} values[50]. Whereas, increasing R_{SSI} values are due to instability of sulfide electrolytes against Li-metal. The rate of interfacial reactions also depends on composition of solid electrolytes along with other factors[47,51], therefore, LPSOI found most stable against Li-metal as compared to LPSOBr and LPSOCl which is good agreement with polarization data of symmetric cells shown in Figure 4.

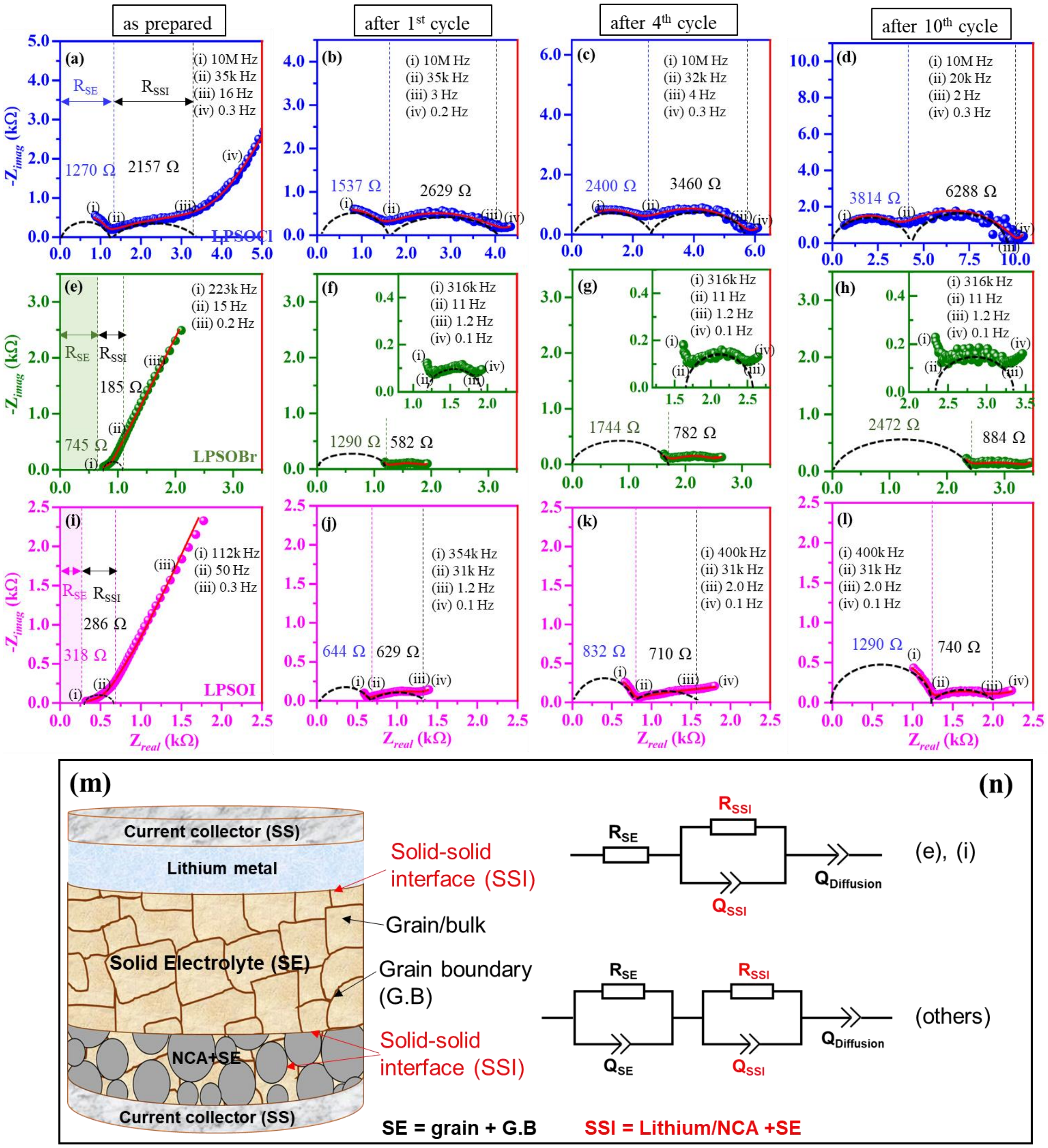

Figure 7. Nyquist plots recorded for as prepared, and after 1st, 4th, and 10th charge-discharge cycle of full solid state battery cell (NCA/SE/Li) of (a-d) LPSOCl, (e-h) LPSOBr, (i-l) LPSOI; (m) Schematic diagram of full solid state battery cell and equivalent circuit used for fitting of different nyquist plots as mentioned in front of each circuit.

To further analyses the impedance of solid electrolyte and effect of pressure relaxation, we have recorded the nyquist plots of LPSOI, LPSOBr and LPSOCl after different time interval from as prepared to 160h. The results show increasing impedance of all three samples with time as shown in Figure S8 of Supporting Information.

The microstructural and elemental analysis of full SSB prepared by LPSOI (cross-sectional view) before (as prepared) and after charge-discharge cycling were measured and results are shown in Figure 8. The thickness of all three layers (anode, cathode and electrolyte) of SSB are shown in micrograph 8(a). The thickness of LPSOI layer is 503 µm, whereas, thickness of anode and cathode composites layers are 127 µm and 91 µm, respectively. SEM-EDX elemental analysis of Ni, C, P, and S are shown in Figure 8 (b & c). Since solid electrolyte LPSOI was mixed in both anode (graphite +SE) and cathode (NCA+SE) composites, therefore, S content is observed in all three layers. Figure 8(d) shows magnified view of cathode composite, and elemental mapping of Ni and S show mixing of NCA and LPSOI in composite as depicted in Figure 8(e & f). A similar microstructures and elemental analysis were performed for anode composite as shown in Figure 8(g-i).

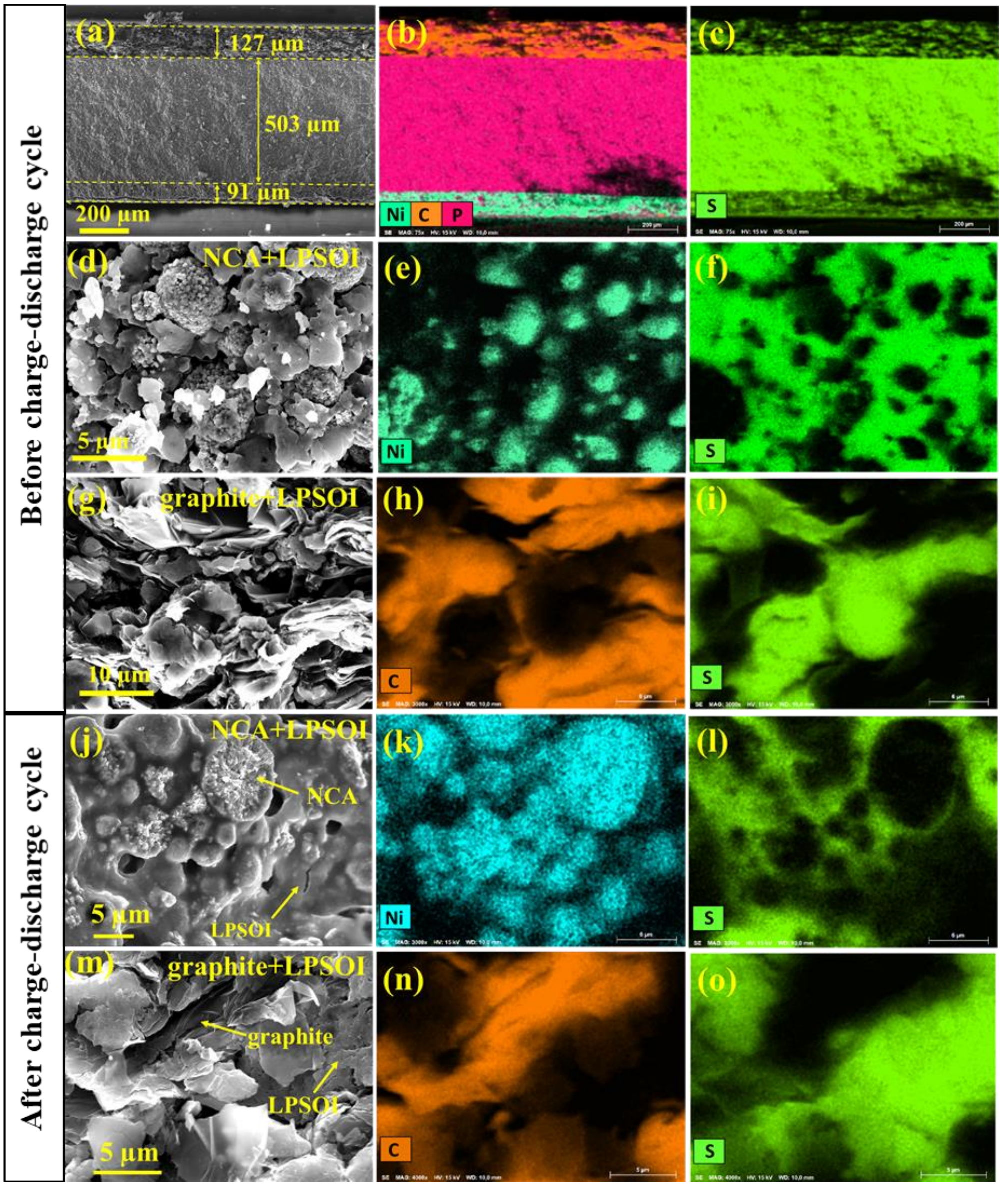

Figure 8. SEM analysis of full SSB (a-i) before charge-discharge cycling, and (j-o) after charge-discharge cycling; (a-c) Microstructure and elemental analysis of full SSB showing all three layers of anode, cathode and electrolytes, (d-f) microstructure and elemental mapping of cathode composite (NCA+LPSOI) before cycling, and (g-i) microstructure and elemental analysis of anode composite (graphite+LPSOI) before cycling, (j-l) Microstructure and elemental mapping of cathode composite after cycling, (m-o) microstructure and elemental mapping of anode composite after cycling.

A postmortem analysis of full SSB of LPSOI was carried out after 20 charge-discharge cycles by SEM and elemental mapping and results are shown in Figure 8(j-o). To performed the postmortem analysis, SSB cell were recovered and cut to see cross-sectional view. Figure 8(j) shows magnified image of composite cathode, and changes in the morphology of composite can be seen clearly. A gel like morphology is observed after cycling, which is different from the fresh composite, may be due to reaction between NCA and LPSOI, and formation of SEI layer. Previous studies also show interfacial reactions between NCA cathode and sulfide electrolytes, and their byproducts such as LiCl, Li_2S, Li_3PO_4, Li_2SO_4 and Ni_3S_4[40,52]. However, solid electrolytes used in reported studies were different than LPSOI but still we can presume similar reactions in our compound. In the elemental mapping of composite, a homogeneous network of solid electrolyte (shown by S mapping) around the NCA particles (shown by Ni mapping) are observed as shown in Figure 8 (k & l).

However, microstructure of anode composite shows more stability between graphite and LPSOI as shown in Figure 8(m), because similar morphology of composite is observed after cycling as it was for as prepared cell. Graphite and LPSOI material are visible in their original state as before cycling. The elemental mapping of graphite (C) and LPSOI (S) are shown in Figures 8(n & o).

During the microstructure analysis of cathode composite in fresh SSB, we have notice the micro gap between NCA particles and LPSOI electrolyte (shown by arrows) as shown in Figures S9 of Supporting information. However, these micro gap were vanished in cathode composite in cycled SSB due to a complete layer of LPSOI was formed over the NCA particles as shown in Figures 7(k & l). These micro gap formed in fresh SSB and gel like layer in cycled SSB could be due to reactivity between NCA and LPSOI[40,52]. Since, there is no reported study available for reference due to our new LPSOI solid electrolyte, therefore, further study by XPS or XAS is required to confirm the reaction products.

Furthermore, interface of solid electrolyte and Li-metal with time was observed by SEM and micrographs are shown in Figure 9. To measure the cross-sectional view, Li foil was mounted on LPSOX pellets at 0.5 Ton (127.5 MPa) of pressure and cut by sharp knife. After cutting, samples were transfer to SEM chamber and recorded the micrographs after 1h, 7h and 68h. We did not observe any changes in the LPSOI-Li interface confirming the stability of the materials. However, we can notice healing of some microcrackes in LPSOCl and LPSOBr (shown by arrows) after 7h and 68h. These changes in the LPSOCl and LPSOBr samples could be relate to the reactivity of materials with Li-metal leading to cracks modification.

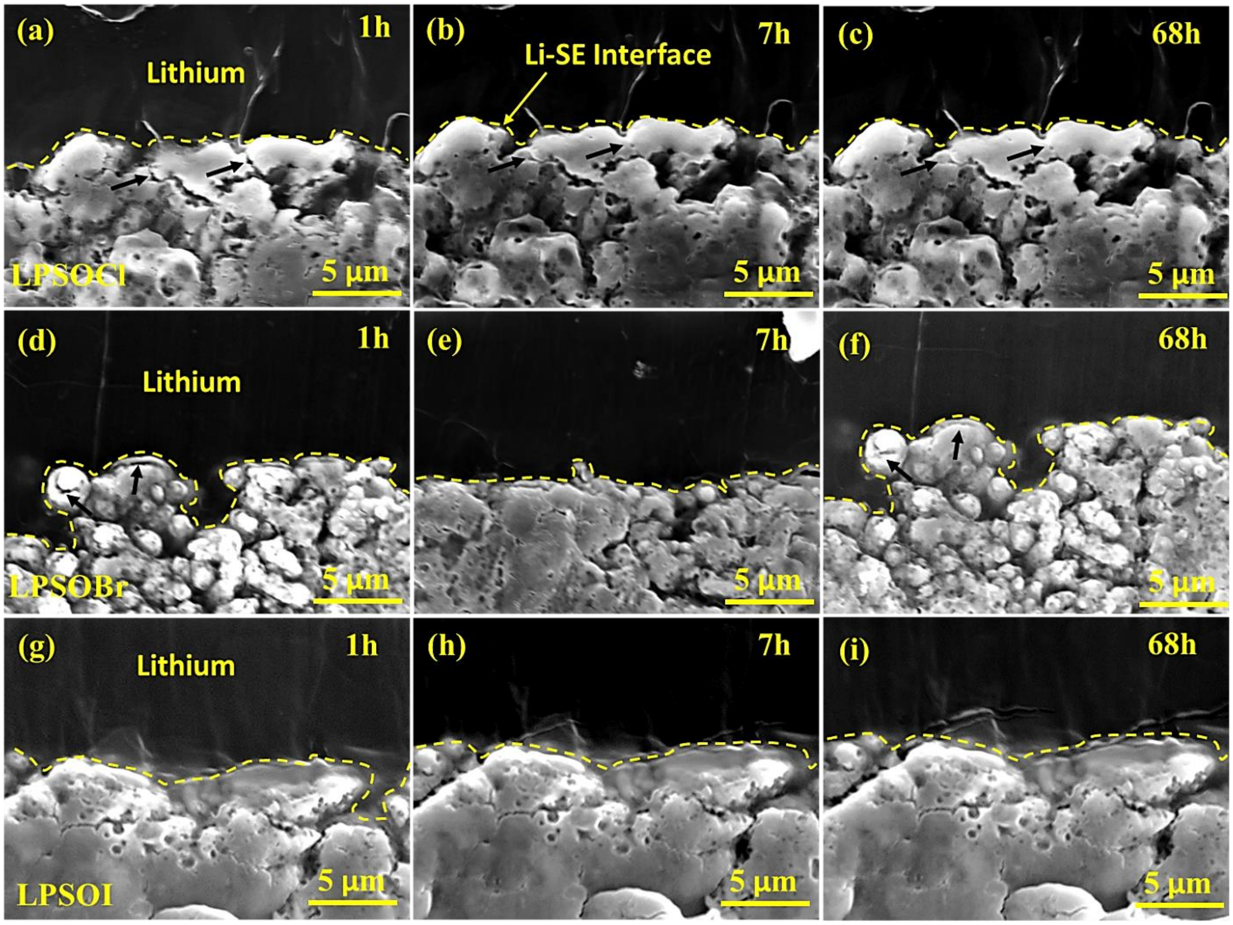

Figure 9. SEM analysis of SE-Li metal interface after 1h, 7h and 68h of contact; (a-c) LPSOCl, (d-f) LPSOBr, and (g-i) LPSOI.

CONCLUSION

In summary, we report a series of new solid electrolytes by halogen (Cl, Br, I) doping in LGPS structured LPSO compound. The study shows Br and I doping increases the lattice volume resulting in additional space for Li-ion diffusion. The iodine-doped sample LPSOI not only shows the highest electrical conductivity of 0.93 mS cm^{-1} but also superior stability against Li metal in the symmetric cell. The higher initial charge-discharge capacities are also found for halogen-doped samples as compared to LPSO. The halogen-doped samples show better stability in the ambient environment as compared to LPSO and LPSOI shows the highest stability on exposure to air and moisture. The *in-situ* EIS study reveals the least interfacial resistance between LPSOI and NCA composite, also, same compound shows lowest interfacial resistance with Li-metal anode in all SEs. A structural and elemental studies were also performed on as prepared and post cycled SSB, and results shows interfacial stability between NCA cathode and LPSOI solid electrolyte. Therefore, halogen especially Br and I doped sulfide electrolytes provides a possible solution to the battery industry for commercializing solid-state batteries.

Supporting Information: Supplementary figures including Refinement pattern and result's table, XRD patterns, SEM-EDS graphs, conductivity graphs, table of conductivity data.

AUTHOR INFORMATION

Authors:

Hari Raj- Normandie Univ, Ensicaen, Unicaen, CNRS, Crismat, 14000 Caen, France;

Réseau sur le Stockage Electrochimique de l'Énergie (RS2E), 80000 Amiens, France.

Email : hari.raj@ensicaen.fr

ORCID: orcid.org/0000-0001-5134-3060

Audric Neveu- Normandie Univ, Ensicaen, Unicaen, CNRS, Crismat, 14000 Caen, France

Email : audric.neveu.kirsch@gmail.com

ORCID: orcid.org/0000-0001-9661-4215

Christian Jordy- SAFT, 111-113 Bd Alfred Daney 33074 Bordeaux, France

Email : christian.jordy@saftbatteries.com

Corresponding Author

Valerie Pralong- Normandie Univ, Ensicaen, Unicaen, CNRS, Crismat, 14000 Caen, France;

Réseau sur le Stockage Electrochimique de l'Énergie (RS2E), 80000 Amiens, France.

Email : valerie.pralong@ensicaen.fr

ORCID: orcid.org/0000-0003-4644-8006

AUTHORS CONTRIBUTIONS

HR has planned and performed all experiments; analyzed the data and written the manuscript draft, AN helped in performing experiments and gave input in manuscript writing, CJ has provided useful solutions and input, and had scientific discussions, VP has checked, and discussed all experimental data and corrected the manuscript. All authors have given approval to the final version of the manuscript.

CONFLICTS OF INTEREST

The authors declare no competing financial interest.

FUNDING SOURCES

Funding was received from the European Union through the Horizon 2020 research and innovation program under the Marie Skłodowska Curie Action grant agreement No. 101034329 and the WINNINGNormandy Program.

ACKNOWLEDGEMENTS

The authors thank Mahima Chaudhary, V. Kovrugin, A. Sagot, S. Duffourt, J. Lecourt, S. Gascoin, H. Laurence, and X. Larose for technical help. Hari Raj and Valerie Pralong gratefully acknowledge the CNRS, Normandy region and European Union for the funding.

REFERENCES

(1) Wang, Q.; Jiang, L.; Yu, Y.; Sun, J. Progress of Enhancing the Safety of Lithium Ion Battery from the Electrolyte Aspect. *Nano Energy* **2019**, *55*, 93–114. https://doi.org/10.1016/J.NANOEN.2018.10.035.

(2) Kim, K.-H.; Martin, S. W. Structures and Properties of Oxygen-Substituted Li 10 SiP 2 S 12−x O x Solid-State Electrolytes. **2019**. https://doi.org/10.1021/acs.chemmater.9b00505.

(3) Janek, J.; Zeier, W. G. A Solid Future for Battery Development. *Nat. Energy 2016 19* **2016**, *1* (9), 1–4. https://doi.org/10.1038/nenergy.2016.141.

(4) Lim, H. D.; Park, J. H.; Shin, H. J.; Jeong, J.; Kim, J. T.; Nam, K. W.; Jung, H. G.; Chung, K. Y. A Review of Challenges and Issues Concerning Interfaces for All-Solid-State Batteries. *Energy Storage Mater.* **2020**, *25*, 224–250. https://doi.org/10.1016/J.ENSM.2019.10.011.

(5) Zhang, B.; Tan, R.; Yang, L.; Zheng, J.; Zhang, K.; Mo, S.; Lin, Z.; Pan, F. Mechanisms and Properties of Ion-Transport in Inorganic Solid Electrolytes. *Energy Storage Mater.* **2018**, *10*, 139–159. https://doi.org/10.1016/J.ENSM.2017.08.015.

(6) Raj, H.; Fabre, T.; Lachal, M.; Neveu, A.; Jean, J.; Steil, M. C.; Bouchet, R.; Pralong, V. Stabilizing the NASICON Solid Electrolyte in an Inert Atmosphere as a Function of Physical Properties and Sintering Conditions for Solid-State Battery Fabrication. *ACS Appl. Energy Mater.* **2023**, *6* (3), 1197–1207. https://doi.org/10.1021/ACSAEM.2C02464/ASSET/IMAGES/LARGE/AE2C02464_0010.JPEG.

(7) Jiang, Z.; Liang, T.; Liu, Y.; Zhang, S.; Li, Z.; Wang, D.; Wang, X.; Xia, X.; Gu, C.; Tu, J. Improved Ionic Conductivity and Li Dendrite Suppression Capability toward Li7P3S11-Based Solid Electrolytes Triggered by Nb and O Cosubstitution. *ACS Appl. Mater. Interfaces* **2020**, *12* (49), 54662–54670.

https://doi.org/10.1021/ACSAMI.0C15903/ASSET/IMAGES/LARGE/AM0C15903_0007.JPEG.

(8) Hayashi, A.; Muramatsu, H.; Ohtomo, T.; Hama, S.; Tatsumisago, M. Improvement of Chemical Stability of Li3PS4 Glass Electrolytes by Adding MxOy (M = Fe, Zn, and Bi) Nanoparticles. *J. Mater. Chem. A* **2013**, *1* (21), 6320–6326. https://doi.org/10.1039/C3TA10247E.

(9) Yu, T.; Ke, B.; Li, H.; Guo, S.; Zhou, H. Recent Advances in Sulfide Electrolytes toward High Specific Energy Solid-State Lithium Batteries. *Mater. Chem. Front.* **2021**, *5* (13), 4892–4911. https://doi.org/10.1039/D1QM00474C.

(10) Kamaya, N.; Homma, K.; Yamakawa, Y.; Hirayama, M.; Kanno, R.; Yonemura, M.; Kamiyama, T.; Kato, Y.; Hama, S.; Kawamoto, K.; Mitsui, A. A Lithium Superionic Conductor. *Nat. Mater. 2011 109* **2011**, *10* (9), 682–686. https://doi.org/10.1038/nmat3066.

(11) Tatsumisago, M.; Nagao, M.; Hayashi, A. Recent Development of Sulfide Solid Electrolytes and Interfacial Modification for All-Solid-State Rechargeable Lithium Batteries. *J. Asian Ceram. Soc.* **2013**, *1* (1), 17–25. https://doi.org/10.1016/J.JASCER.2013.03.005.

(12) Neveu, A.; Pelé, V.; Jordy, C.; Pralong, V. Exploration of Li–P–S–O Composition for Solid-State Electrolyte Materials Discovery. *J. Power Sources* **2020**, *467*, 228250. https://doi.org/10.1016/J.JPOWSOUR.2020.228250.

(13) Wan, H.; Liu, S.; Deng, T.; Xu, J.; Zhang, J.; He, X.; Ji, X.; Yao, X.; Wang, C. Bifunctional Interphase-Enabled Li10GeP2S12Electrolytes for Lithium-Sulfur Battery. *ACS Energy Lett.* **2021**, *6* (3), 862–868. https://doi.org/10.1021/ACSENERGYLETT.0C02617/ASSET/IMAGES/LARGE/NZ0C02617_0007.JPEG.

(14) Richards, W. D.; Miara, L. J.; Wang, Y.; Kim, J. C.; Ceder, G. Interface Stability in Solid-State Batteries. *Chem. Mater.* **2016**, *28* (1), 266–273.

https://doi.org/10.1021/ACS.CHEMMATER.5B04082/ASSET/IMAGES/LARGE/CM-2015-04082X_0005.JPEG.

(15) Bron, P.; Johansson, S.; Zick, K.; Der Günne, J. S. A.; Dehnen, S.; Roling, B. Li10SnP2S12: An Affordable Lithium Superionic Conductor. *J. Am. Chem. Soc.* **2013**, *135* (42), 15694–15697. https://doi.org/10.1021/JA407393Y/SUPPL_FILE/JA407393Y_SI_002.CIF.

(16) Kuhn, A.; Gerbig, O.; Zhu, C.; Falkenberg, F.; Maier, J.; Lotsch, B. V. A New Ultrafast Superionic Li-Conductor: Ion Dynamics in Li 11 Si 2 PS 12 and Comparison with Other Tetragonal LGPS-Type Electrolytes. *Phys. Chem. Chem. Phys.* **2014**, *16* (28), 14669–14674. https://doi.org/10.1039/C4CP02046D.

(17) Bron, P.; Dehnen, S.; Roling, B. Li10Si0.3Sn0.7P2S12 – A Low-Cost and Low-Grain-Boundary-Resistance Lithium Superionic Conductor. *J. Power Sources* **2016**, *329*, 530–535. https://doi.org/10.1016/J.JPOWSOUR.2016.08.115.

(18) Bron, P.; Roling, B.; Dehnen, S. Impedance Characterization Reveals Mixed Conducting Interphases between Sulfidic Superionic Conductors and Lithium Metal Electrodes. *J. Power Sources* **2017**, *352*, 127–134. https://doi.org/10.1016/J.JPOWSOUR.2017.03.103.

(19) Kato, Y.; Hori, S.; Saito, T.; Suzuki, K.; Hirayama, M.; Mitsui, A.; Yonemura, M.; Iba, H.; Kanno, R. High-Power All-Solid-State Batteries Using Sulfide Superionic Conductors. *Nat. Energy 2016 14* **2016**, *1* (4), 1–7. https://doi.org/10.1038/nenergy.2016.30.

(20) Ito, T.; Hori, S.; Hirayama, M.; Kanno, R. Liquid-Phase Synthesis of the Li10GeP2S12-Type Phase in the Li–Si–P–S–Cl System. *J. Mater. Chem. A* **2022**, *10* (27), 14392–14398. https://doi.org/10.1039/D2TA02834D.

(21) Song, S.; Hori, S.; Li, Y.; Suzuki, K.; Matsui, N.; Hirayama, M.; Saito, T.; Kamiyama, T.; Kanno, R. Material Search for a Li10GeP2S12-Type Solid Electrolyte in the Li-P-S-X (X = Br, I) System via

Clarification of the Composition-Structure-Property Relationships. *Chem. Mater.* **2022**, *34* (18), 8237–8247. https://doi.org/10.1021/ACS.CHEMMATER.2C01608/ASSET/IMAGES/LARGE/CM2C01608_0009.JPEG.

(22) He, Y.; Chen, W.; Zhao, Y.; Li, Y.; Lv, C.; Li, H.; Yang, J.; Gao, Z.; Luo, J. Recent Developments and Progress of Halogen Elements in Enhancing the Performance of All-Solid-State Lithium Metal Batteries. *Energy Storage Mater.* **2022**, *49*, 19–57. https://doi.org/10.1016/J.ENSM.2022.03.043.

(23) Suzuki, K.; Sakuma, M.; Hori, S.; Nakazawa, T.; Nagao, M.; Yonemura, M.; Hirayama, M.; Kanno, R. Synthesis, Structure, and Electrochemical Properties of Crystalline Li–P–S–O Solid Electrolytes: Novel Lithium-Conducting Oxysulfides of Li10GeP2S12 Family. *Solid State Ionics* **2016**, *288*, 229–234. https://doi.org/10.1016/J.SSI.2016.02.002.

(24) Shannon, R. D.; IUCr. Revised Effective Ionic Radii and Systematic Studies of Interatomic Distances in Halides and Chalcogenides. *urn:issn:0567-7394* **1976**, *32* (5), 751–767. https://doi.org/10.1107/S0567739476001551.

(25) Tarhouchi, I.; Viallet, V.; Vinatier, P.; Ménétrier, M. Electrochemical Characterization of Li10SnP2S12: An Electrolyte or a Negative Electrode for Solid State Li-Ion Batteries? *Solid State Ionics* **2016**, *296*, 18–25. https://doi.org/10.1016/j.ssi.2016.08.016.

(26) Mulder, W. H.; Sluyters, J. H.; Pajkossy, T.; Nyikos, L. Tafel Current at Fractal Electrodes. Connection with Admittance Spectra. *J. Electroanal. Chem.* **1990**, *285* (1–2), 103–115. https://doi.org/10.1016/0022-0728(90)87113-X.

(27) Zhang, L.; Dai, Y.; Li, C.; Dang, Y.; Zheng, R.; Wang, Z.; Wang, Y.; Cui, Y.; Arandiyan, H.; Shao, Z.; Sun, H.; Zhuang, Q.; Liu, Y. Recent Advances in Electrochemical Impedance Spectroscopy for Solid-State Batteries. *Energy Storage Mater.* **2024**, *69* (March).

https://doi.org/10.1016/j.ensm.2024.103378.

(28) Irvine, J. T. S.; Sinclair, D. C.; West, A. R. Electroceramics: Characterization by Impedance Spectroscopy. *Adv. Mater.* **1990**, *2* (3), 132–138. https://doi.org/10.1002/adma.19900020304.

(29) Brug, G. J.; van den Eeden, A. L. G.; Sluyters-Rehbach, M.; Sluyters, J. H. The Analysis of Electrode Impedances Complicated by the Presence of a Constant Phase Element. *J. Electroanal. Chem.* **1984**, *176* (1–2), 275–295. https://doi.org/10.1016/S0022-0728(84)80324-1.

(30) Bron, P.; Dehnen, S.; Roling, B. Li10Si0.3Sn0.7P2S12 – A Low-Cost and Low-Grain-Boundary-Resistance Lithium Superionic Conductor. *J. Power Sources* **2016**, *329*, 530–535. https://doi.org/10.1016/j.jpowsour.2016.08.115.

(31) Kim, K. S.; Rajagopal, R.; Ryu, K. S. The Improvement of Electrochemical Performance by Mixing InF3 in Li5.3PS4.3Cl1.7 Solid Electrolyte. *J. Alloys Compd.* **2024**, *992* (April), 174620. https://doi.org/10.1016/j.jallcom.2024.174620.

(32) Doux, J. M.; Yang, Y.; Tan, D. H. S.; Nguyen, H.; Wu, E. A.; Wang, X.; Banerjee, A.; Meng, Y. S. Pressure Effects on Sulfide Electrolytes for All Solid-State Batteries. *J. Mater. Chem. A* **2020**, *8* (10), 5049–5055. https://doi.org/10.1039/c9ta12889a.

(33) Lu, Y.; Zhao, C. Z.; Yuan, H.; Cheng, X. B.; Huang, J. Q.; Zhang, Q. Critical Current Density in Solid-State Lithium Metal Batteries: Mechanism, Influences, and Strategies. *Adv. Funct. Mater.* **2021**, *31* (18), 2009925. https://doi.org/10.1002/ADFM.202009925.

(34) Sudo, R.; Nakata, Y.; Ishiguro, K.; Matsui, M.; Hirano, A.; Takeda, Y.; Yamamoto, O.; Imanishi, N. Interface Behavior between Garnet-Type Lithium-Conducting Solid Electrolyte and Lithium Metal. *Solid State Ionics* **2014**, *262*, 151–154. https://doi.org/10.1016/J.SSI.2013.09.024.

(35) Raj, R.; Wolfenstine, J. Current Limit Diagrams for Dendrite Formation in Solid-State Electrolytes

for Li-Ion Batteries. *J. Power Sources* **2017**, *343*, 119–126. https://doi.org/10.1016/J.JPOWSOUR.2017.01.037.

(36) Li, J.; Liu, W.; Zhang, X.; Ma, Y.; Wei, Y.; Fu, Z.; Li, J.; Yan, Y. Heat Treatment Effects in Oxygen-Doped β-Li3PS4 Solid Electrolyte Prepared by Wet Chemistry Method. *J. Solid State Electrochem.* **2021**, *25* (4), 1259–1269. https://doi.org/10.1007/S10008-021-04904-2/FIGURES/8.

(37) Bach, P.; Stratmann, M.; Valencia-Jaime, I.; Romero, A. H.; Renner, F. U. Lithiation and Delithiation Mechanisms of Gold Thin Film Model Anodes for Lithium Ion Batteries: Electrochemical Characterization. *Electrochim. Acta* **2015**, *164*, 81–89. https://doi.org/10.1016/J.ELECTACTA.2015.02.184.

(38) Bach, P.; Valencia-Jaime, I.; Rütt, U.; Gutowski, O.; Romero, A. H.; Renner, F. U. Electrochemical Lithiation Cycles of Gold Anodes Observed by in Situ High-Energy X-Ray Diffraction. *Chem. Mater.* **2016**, *28* (9), 2941–2948. https://doi.org/10.1021/ACS.CHEMMATER.5B04719/ASSET/IMAGES/LARGE/CM-2015-047194_0007.JPEG.

(39) Sakuma, M.; Suzuki, K.; Hirayama, M.; Kanno, R. Reactions at the Electrode/Electrolyte Interface of All-Solid-State Lithium Batteries Incorporating Li–M (M = Sn, Si) Alloy Electrodes and Sulfide-Based Solid Electrolytes. *Solid State Ionics* **2016**, *285*, 101–105. https://doi.org/10.1016/J.SSI.2015.07.010.

(40) Banerjee, A.; Tang, H.; Wang, X.; Cheng, J. H.; Nguyen, H.; Zhang, M.; Tan, D. H. S.; Wynn, T. A.; Wu, E. A.; Doux, J. M.; Wu, T.; Ma, L.; Sterbinsky, G. E.; D'Souza, M. S.; Ong, S. P.; Meng, Y. S. Revealing Nanoscale Solid-Solid Interfacial Phenomena for Long-Life and High-Energy All-Solid-State Batteries. *ACS Appl. Mater. Interfaces* **2019**, *11* (46), 43138–43145. https://doi.org/10.1021/ACSAMI.9B13955/ASSET/IMAGES/LARGE/AM9B13955_0008.JPEG.

(41) Muramatsu, H.; Hayashi, A.; Ohtomo, T.; Hama, S.; Tatsumisago, M. Structural Change of Li2S-P2S5 Sulfide Solid Electrolytes in the Atmosphere. *Solid State Ionics* **2011**, *182* (1), 116–119. https://doi.org/10.1016/j.ssi.2010.10.013.

(42) Khurram Tufail, M.; Ahmad, N.; Zhou, L.; Faheem, M.; Yang, L.; Chen, R.; Yang, W. Insight on Air-Induced Degradation Mechanism of Li7P3S11 to Design a Chemical-Stable Solid Electrolyte with High Li2S Utilization in All-Solid-State Li/S Batteries. *Chem. Eng. J.* **2021**, *425* (March), 130535. https://doi.org/10.1016/j.cej.2021.130535.

(43) Xu, M.; Song, S.; Daikuhara, S.; Matsui, N.; Hori, S.; Suzuki, K.; Hirayama, M.; Shiotani, S.; Nakanishi, S.; Yonemura, M.; Saito, T.; Kamiyama, T.; Kanno, R. Li10GeP2S12-Type Structured Solid Solution Phases in the Li9+δP3+δ′S12-KOkSystem: Controlling Crystallinity by Synthesis to Improve the Air Stability. *Inorg. Chem.* **2022**, *61* (1), 52–61. https://doi.org/10.1021/acs.inorgchem.1c01748.

(44) Neveu, A.; Raj, H.; Pelé, V.; Jordy, C.; Pralong, V. Effect of the Boron Element in a Li-P-S System. *Dalt. Trans.* **2023**, *52* (47), 18045–18052. https://doi.org/10.1039/d3dt02883f.

(45) Gaberšček, M. Understanding Li-Based Battery Materials via Electrochemical Impedance Spectroscopy. *Nat. Commun.* **2021**, *12* (1), 19–22. https://doi.org/10.1038/s41467-021-26894-5.

(46) Moškon, J.; Žuntar, J.; Drvarič Talian, S.; Dominko, R.; Gaberšček, M. A Powerful Transmission Line Model for Analysis of Impedance of Insertion Battery Cells: A Case Study on the NMC-Li System. *J. Electrochem. Soc.* **2020**, *167* (14), 140539. https://doi.org/10.1149/1945-7111/abc769.

(47) Hori, S.; Kanno, R.; Sun, X.; Song, S.; Hirayama, M.; Hauck, B.; Dippon, M.; Dierickx, S.; Ivers-Tiffée, E. Understanding the Impedance Spectra of All-Solid-State Lithium Battery Cells with Sulfide Superionic Conductors. *J. Power Sources* **2023**, *556* (November 2022). https://doi.org/10.1016/j.jpowsour.2022.232450.

(48) Shin, M.; Gewirth, A. A. Incorporating Solvate and Solid Electrolytes for All-Solid-State Li2S Batteries with High Capacity and Long Cycle Life. *Adv. Energy Mater.* **2019**, *9* (26), 1–11. https://doi.org/10.1002/aenm.201900938.

(49) Wenzel, S.; Randau, S.; Leichtweiß, T.; Weber, D. A.; Sann, J.; Zeier, W. G.; Janek, J. Direct Observation of the Interfacial Instability of the Fast Ionic Conductor Li10GeP2S12 at the Lithium Metal Anode. *Chem. Mater.* **2016**, *28* (7), 2400–2407. https://doi.org/10.1021/acs.chemmater.6b00610.

(50) Yamauchi, H.; Ikejiri, J.; Tsunoda, K.; Tanaka, A.; Sato, F.; Honma, T.; Komatsu, T. Enhanced Rate Capabilities in a Glass-Ceramic-Derived Sodium All-Solid-State Battery. *Sci. Rep.* **2020**, *10* (1), 1–12. https://doi.org/10.1038/s41598-020-66410-1.

(51) Sakuda, A.; Kitaura, H.; Hayashi, A.; Tadanaga, K.; Tatsumisago, M. Modification of Interface Between LiCoO[Sub 2] Electrode and Li[Sub 2]S–P[Sub 2]S[Sub 5] Solid Electrolyte Using Li[Sub 2]O–SiO[Sub 2] Glassy Layers. *J. Electrochem. Soc.* **2009**, *156* (1), A27. https://doi.org/10.1149/1.3005972.

(52) Kwak, H. W.; Park, Y. J. Cathode Coating Using LiInO2-LiI Composite for Stable Sulfide-Based All-Solid-State Batteries. *Sci. Reports 2019 91* **2019**, *9* (1), 1–9. https://doi.org/10.1038/s41598-019-44629-x.